The Astrophysical Journal, 668:23–44, 2007 October 10

MORPHOLOGIES OF GALAXIES IN AND AROUND A PROTOCLUSTER AT $z = 2.300$

Annika H. G. Peter
Department of Physics, Princeton University, Princeton, NJ 08544

Alice E. Shapley
Department of Astrophysical Sciences, Princeton University, Princeton, NJ 08544

David R. Law and Charles C. Steidel
California Institute of Technology, MS 105-24, Pasadena, CA 91125

Dawn K. Erb
Harvard-Smithsonian Center for Astrophysics, Cambridge, MA 02138

Naveen A. Reddy
National Optical Astronomy Observatory, Tuscon, AZ 85719

and

Max Pettini
Institute of Astronomy, University of Cambridge, Cambridge CB3 0HA, UK
Received 2007 February 27; accepted 2007 June 16

ABSTRACT

We present results from the first robust investigation of galaxy morphology as a function of environment at $z > 1.5$. Our study is motivated by the fact that star-forming galaxies contained within a protocluster at $z = 2.3$ in the HS 1700+64 field have significantly older ages and larger stellar masses on average than those at similar redshifts but more typical environmental densities. In the analysis of *HST* ACS images, we apply nonparametric statistics to characterize the rest-frame UV morphologies of a sample of 85 UV-selected star-forming galaxies at $z = 1.7$–2.9, 22 of which are contained in the protocluster. The remaining 63 control sample galaxies are not in the protocluster but have a similar mean redshift of $\bar{z} \sim 2.3$. We find no environmental dependence for the distributions of morphological properties. Combining the measured morphologies with the results of population synthesis modeling, we find only weak correlations, if any, between morphological and stellar population properties such as stellar mass, age, extinction, and star formation rate. Given the incomplete census of the protocluster galaxy population, and the lack of correlation between rest-frame UV morphology and star formation history at $z \sim 2$ within our sample, the absence of environmental trends in the distribution of morphological properties is not surprising. In addition, using a larger sample of photometric candidates, we compare morphological distributions for 282 UV-selected and 43 near-IR-selected galaxies. While the difference in the degree of nebulosity between the two samples appears to be a by-product of the fainter average rest-frame UV surface brightness of the near-IR-selected galaxies, we find that, among the lowest surface brightness galaxies, the near-IR-selected objects have significantly smaller angular sizes.

Subject headings: cosmology: observations — galaxies: clusters: general — galaxies: high-redshift — galaxies: structure

Online material: color figures

1. INTRODUCTION

Galaxies populate the local universe in a very regular way. Dynamically hot elliptical galaxies are found preferentially in large galaxy clusters, especially the very centers (Dressler 1980; Postman & Geller 1984; Goto et al. 2003). Dynamically cold spiral galaxies tend to lie in the less dense environments of groups or the field. The name given for these trends is the ''morphology-density'' relation. The morphology-density relation is already in place by $z = 1$, although there are quantitative, but not qualitative, differences between $z = 1$ and $z = 0$ (Postman et al. 2005; Smith et al. 2005). For example, the elliptical fraction in clusters is lower at $z = 1$ than at $z = 0$, but the cluster elliptical fraction is higher than the elliptical fraction in the field in both epochs. One of the outstanding problems in the theory of galaxy evolution and structure formation is understanding when and how this relation is established.

The morphology-density relation is entangled with several other observed relations between physical properties of galaxies and their classification and environment. In the local universe, elliptical galaxies are structurally different and, on average, have higher mass, less active star formation (as well as less gas available for star formation), and redder colors than spiral galaxies (Kauffmann et al. 2003). Therefore, in addition to a morphology-density relation, strong trends of galaxy color with environment are observed in the Sloan Digital Sky Survey (SDSS; Kauffmann et al. 2004; Blanton et al. 2005). These trends have been traced out to $z = 1.3$ with the Deep Extragalactic Evolutionary Probe 2 (DEEP2) galaxy redshift survey (Davis et al. 2003; Cooper et al. 2006, 2007; Gerke et al. 2007). Studies of the local universe strongly imply that the correlations between color and star formation history and environment are more fundamental than the morphology-density relation (Kauffmann et al. 2004; Blanton et al. 2005). As part of the program of understanding galaxy evolution, it is important to explain the relation between the physical structure of galaxies and their star formation history, and the correlations between the various galactic properties and environment.

There are many theories to explain how such correlations arise as part of the hierarchical picture of structure formation. Several authors have considered how much of the morphology-density relation is simply a result of the merger histories of the host halos. Benson et al. (2001) graft semianalytic models onto a cosmological dark matter *N*-body simulation (Jenkins et al. 1998; Kauffmann et al. 1999) and examine the resulting morphology-density and color-density relations at the current epoch. They find qualitative agreement with observations of the early-type fraction and average galaxy color as a function of environment. Their semianalytic model overpredicts the red fraction at the center of clusters, and underpredicts the number of spheroids in the field at $z = 1$ (Benson et al. 2002). Okamoto & Nagashima (2001) also use semianalytic models to interpret their dark matter simulations, but focus only on the morphology-density relation within clusters. While they can reproduce the elliptical fraction as a function of density with their semianalytic prescription, the modeled S0 fraction does not agree with observations. Using a simple prescription for the relationship between the host dark matter halo mass accretion history and galaxies lying in the halos, Maulbetsch et al. (2007) are able to qualitatively, but not quantitatively, reproduce the morphology-density and specific star formation rate environmental correlation at $z = 0$. In addition, the predicted morphology-density relation predicted at $z = 1$ differs dramatically from what is observed at that redshift. Therefore, while it is likely that the merger history influences the correlations among environment, star formation history, and morphology, it is not the only driver.

In particular, a number of baryonic processes are invoked to explain these correlations. Each process is associated with a characteristic timescale and halo mass, producing different effects on the photometric and structural properties of either central or satellite galaxies. Central galaxies continue to form stars as long as they can accrete significant amounts of cold gas. Cosmological simulations suggest that gas can cool in halos of $M < 10^{12}\ M_{\odot}$ up to the current epoch, but not in more massive halos since $z \sim 2$ (Kereš et al. 2005; Croton et al. 2006; Dekel & Birnboim 2006). This trend translates directly into the color distributions of the associated galaxies, but there is no prediction for how the gas accretion history specifically affects morphology evolution. Satellite galaxies falling into more massive halos are subject to a number of processes, such as ram pressure stripping (Gunn & Gott 1972; Abadi et al. 1999; Hester 2006), "strangulation" or "starvation" (Larson et al. 1980; Bekki et al. 2002), and harassment due to high-speed encounters with other galaxies (Moore et al. 1996, 1999). The relative importance of these mechanisms for altering morphology depends on both properties of the satellite galaxies and the larger host halo.

Disentangling these processes is extremely difficult, since galaxies can experience most of them during some point in their evolution. In order to determine which processes drive the morphology-density, color-density, and star formation–density relations, it is important to observe galaxies in a range of environments at a variety of epochs, in which different processes may dominate. In particular, since many theories on galaxy evolution focus on processes that are most likely to be effective in cluster environments, where the environmental contrast is maximized, it is important to observe clusters in different stages of formation, even before the structures have virialized.

Several high-redshift galaxy overdensities have been observed that are thought to virialize into massive clusters by the current epoch. Commonly called "protoclusters," some of these objects have been found serendipitously (Pascarelle et al. 1996; Steidel et al. 1998, 2005). Others were discovered through narrowband Lyα and Hα surveys targeting the regions about high-redshift radio galaxies (HzRGs; Kurk et al. 2002; Overzier et al. 2006) because HzRGs lie in highly biased environments (De Breuck et al. 2000). One of the best-established (and most thoroughly observed) protoclusters is at $z = 2.300$ in the Q1700 field centered on the HS 1700+643 quasar, and was discovered in a survey of $z = 2.4 \pm 0.4$ star-forming galaxies in that field (Steidel et al. 2004, 2005). Spectroscopy of >100 photometric $z > 1.5$ candidates in the Q1700 field allows this structure to be well mapped in projected and redshift space, and leads to a good estimate of the mass overdensity. This stands in contrast to work on the other protoclusters, for which the estimated mass overdensity is based on projected number densities of Lyα emitters, which do not fully trace the underlying population of high-redshift galaxies, and for which the number density in average environments is not well quantified. Furthermore, protocluster membership for galaxies that are not Lyα emitters is established using photometric redshifts, which have large $\delta(z) \geq 0.5$ errors (Overzier et al. 2006). The mass overdensity of the Q1700 protocluster indicates that it should virialize into a massive cluster of $\sim 1.4 \times 10^{15}\ M_{\odot}$ by the present (Steidel et al. 2005).

Stellar population synthesis modeling of the deep multiband photometry and spectroscopy of the star-forming galaxies in the Q1700 field indicate that galaxies in the protocluster are, on average, significantly more massive and older than galaxies in the field. Complementary analyses of the spatial clustering of $z > 2$ galaxies as a function of rest-frame optical color suggest that redder galaxies are more strongly clustered (Adelberger et al. 2005a; Quadri et al. 2007), which is consistent with the results from the Q1700 protocluster. Therefore, it appears that star formation history is already a strong function of environment at high redshift.

In this paper, we explore connections between morphology and environment, and morphology and star formation history at high redshift. We examine the rest-UV morphologies of optically selected, spectroscopically confirmed star-forming galaxies in the Q1700 field, performing the first rigorous analysis of morphology as a function of environment at $z > 1.3$. In addition, given the large multiband data set available for this field, we are able to identify a complementary population of high-redshift galaxies selected by their near-IR colors, and compare their properties with those of the UV-selected galaxies. The structure of the paper is as follows: in § 2 we summarize previous observations of the Q1700 field and present our new *Hubble Space Telescope* Advanced Camera for Surveys (*HST* ACS) observations, from which we derive morphologies for our galaxy sample. In § 3 we describe the set of parameters we use to quantify morphology, and present tests of the robustness of these parameters. We discuss the results of the analysis on the environmental dependence on morphology for star-forming galaxies in § 4. We present an analysis of morphology as a function of star formation history and the physical properties of galaxies in § 5. In § 6 we compare the distributions of morphological parameters of optically and near-IR selected galaxies. We discuss the results of our analyses and place them in the broader picture of structure formation and galaxy evolution in § 7.

For the rest of this paper, we assume a flat cosmology with $\Omega_m = 0.3$, $\Omega_{\Lambda} = 0.7$, and $h = 0.7$.

2. OBSERVATIONS AND SAMPLE SELECTION

2.1. *Prior Observations*

In order to optically select high-redshift star-forming galaxies in the foreground of the HS 1700+643 quasar, Steidel et al. (2004) observed a $15.3' \times 15.3'$ field (Q1700) with the Prime

Focus Imager on the William Herschel Telescope in the U_n, G, and $\mathcal{R}$ bands, with supplementary observations using the U_n filter with the Low Resolution Imaging Spectrometer (LRIS) on the Keck I telescope.

Spectroscopic follow-up was concentrated on the region nearest the HS 1700+643 quasar. Redshifts were primarily measured from optical spectra probing the rest-frame UV. These spectra were obtained using the LRIS-B instrument on the Keck I telescope (Steidel et al. 2004). In addition, Erb et al. (2006) measured Hα redshifts for 19 objects in the larger optical spectroscopic sample using the NIRSPEC near-IR spectrograph on Keck II. In total, 167 galaxy photometric candidates have secure redshifts, of which 141 have $z > 1.4$. The contaminants were stars and low-redshift galaxies. The current Q1700 spectroscopic sample is larger than the original one presented in Steidel et al. (2005) due to subsequent additional observations.

In order to perform population synthesis modeling on those galaxies with secure redshifts, near- and mid-IR observations of the Q1700 field were performed and presented by Barmby et al. (2004), Shapley et al. (2005), and Erb et al. (2006). Data in the 3.5–8.0 μm wave bands were obtained with the Infrared Array Camera (IRAC) on the *Spitzer Space Telescope* during the In-Orbit Checkout. Data reductions and photometry are described in Barmby et al. (2004) and Shapley et al. (2005). Using WIRC (Wide Field Imaging Camera) on the 5 m Palomar Hale telescope, a $8.5' \times 8.5'$ section of the Q1700 field was imaged in the J and K_s (Erb et al. 2006; Shapley et al. 2005) bands. These data also allow us to identify a sample of distant red galaxies ("DRGs") satisfying the $J-K_s > 2.3$ criterion of Franx et al. (2003). This selection criterion is tuned to select galaxies with significant 4000 Å/Balmer breaks at $z \approx 2.5$, and hence, selects galaxies with either old or heavily obscured stellar populations (Förster Schreiber et al. 2004; van Dokkum et al. 2004; Reddy et al. 2005).

2.2. *HST ACS Observations*

We imaged the Q1700 field with the *HST* ACS using the F814W filter. For a protocluster mean redshift of $z = 2.300$, the pivot wavelength of the filter corresponds to a rest-frame wavelength of $\lambda \sim 2500$ Å, and the FWHM of the point-spread function of $0.12''$ corresponds to $\approx$1 kpc at $z = 2.3$. In order to include as many of the spectroscopically confirmed galaxies as possible, we covered the region nearest the HS 1700+643 quasar with four pointings (Fig. 1). Each pointing was imaged over the course of five orbits of nearly equal exposure time, for a total exposure time of 12520 s. This corresponds to a sensitivity of 29.0 AB magnitude for a 1 σ surface brightness fluctuation in a 1 arcsec^2 aperture, and a 28.4 AB magnitude depth for a 10 σ point source in a $0.1''$ radius circular aperture. We used the MultiDrizzle script (Koekemoer et al. 2002) to clean, sky subtract, and drizzle the flat-fielded data products from the ACS CALACS software pipeline. In order to align the ACS image to the ground-based coordinate system, we used $\approx$100 bright objects on each pointing to create a map between the ACS and ground-based coordinate systems. We then corrected the ACS image world coordinate system accordingly.

2.3. *Sample Selection*

High-redshift photometric candidate galaxies were selected using the BX/MD/C/D/M photometric color selection schemes of Steidel et al. (2003) and Adelberger et al. (2004). A total of 1472 "BX", 238 "MD", 81 "C", 74 "D", and 45 "M" candidate galaxies were identified in the optical ground-based observations of the Q1700 field, for a total of 1910 optically selected galaxy candidates (Steidel et al. 2004, 2005). Of primary interest to us for our environmental study of the $z = 2.300$ galaxy redshift spike ("protocluster") are the BX/MD objects, for which the mean redshifts are $z = 2.20$ and $z = 2.79$, respectively (Steidel et al. 2003; Adelberger et al. 2004), in contrast to the mean redshift $z \approx 3$ for the combined C/D/M sample. As discussed in § 2.1, 141 of these galaxies have secure redshifts, of which 25 are in the overdensity. In the near-IR field, we identified 75 DRGs, 11 of which are also classified as BX or MD objects. Of the DRGs that are also classified as BX or MD objects, seven have spectroscopic redshifts, of which two are in the overdensity. Figure 1 illustrates the footprints of all the observations and all of the galaxy samples.

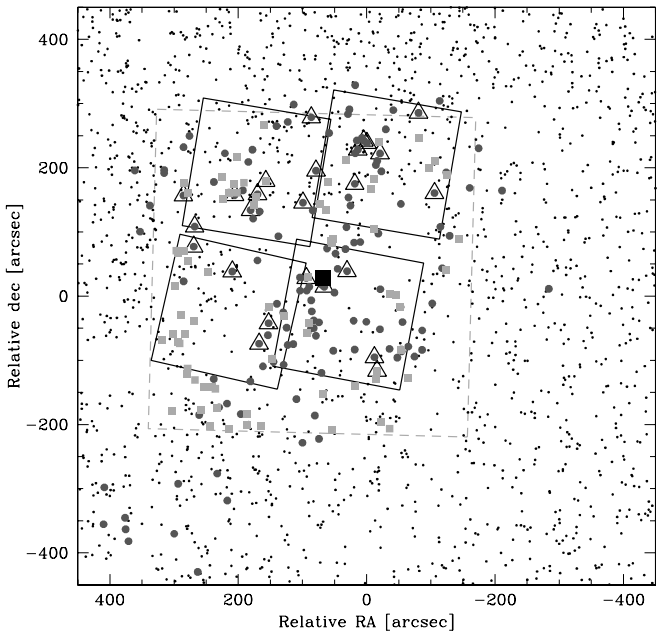

FIG. 1.—Schematic of observations and samples. The image covers the full scale of the $\mathcal{R}$-band observation. The K_s observation is bounded by the dashed box. The *HST* ACS footprint is denoted by the four black-rimmed boxes. Marked by the large filled square is the HS 1700+643 quasar. Objects that satisfy the rest-frame UV color criteria but for which no redshift information is available are marked by small dots; those with redshift information are denoted by large dots, with triangles about the spike objects. DRGs are marked with gray squares. Objects satisfying more than one selection criterion will have stacked markers. [*See the electronic edition of the Journal for a color version of this figure.*]

A total of 22 of 25 BX/MD objects whose spectroscopic redshifts place them in the protocluster fell on the footprint of our ACS observations. In addition, 72 optically selected objects with redshifts $z > 1.7$ but not within the protocluster were observed by ACS, as were 234 BX/MD/C/D/M objects without spectroscopic redshifts (of which 223 are not obviously stars or large foreground galaxies) and 43 DRGs. Figures 2–5 show images of the spectroscopically confirmed optically selected galaxies, and all the DRGs. All seven of the DRGs that also satisfy optical selection criteria and have spectroscopic redshifts are on the ACS pointings, as are three of the four DRGs that are also BX or MD objects that do not have secure redshifts. A summary of the ACS galaxy samples can be found in Table 1.

3. MORPHOLOGICAL PARAMETERS

3.1. *Parameter Choice*

Galaxies at $z \sim 2$ are not easily classified by the Hubble sequence. As demonstrated in Figures 2–5, and as noted in previous

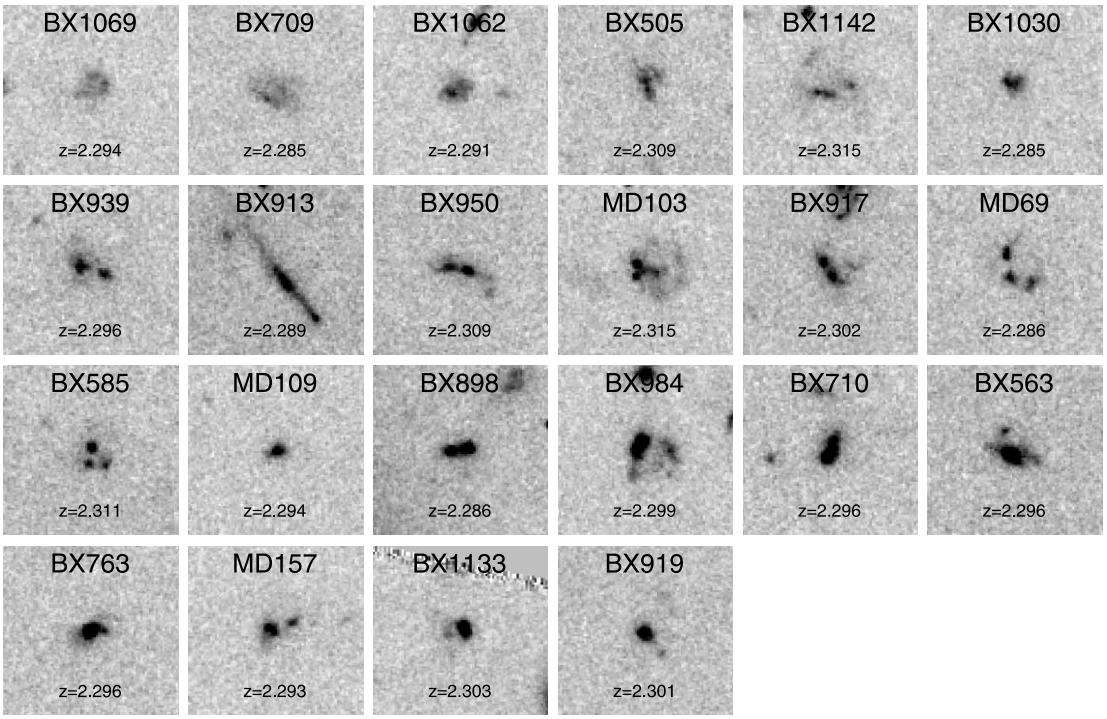

FIG. 2.—*HST* ACS images of galaxies spectroscopically confirmed to be in the protocluster, sorted in order of increasing Gini. Each thumbnail is $4'' \times 4''$ in size. Images are centered at the centroid of the $\mathcal{R}$-band isophotes. The elongated morphology of BX 913 may be due to lensing by the foreground X-ray cluster RX J1701.3+6414 at $z = 0.453$ (Mullis et al. 2003).

studies of the rest-frame UV and optical morphologies of $z > 2$ galaxies (e.g., Dickinson 2000; Elmegreen et al. 2004b; Lotz et al. 2006; Law et al. 2007), high-redshift galaxies tend to be clumpy and highly irregular, with no strong evidence for spiral or elliptical types. Therefore, there have been several attempts to define a set of quantitative measures of morphology. Some (e.g., Ravindranath et al. 2006; Zirm et al. 2007) have used circularly symmetric Sérsic fits to quantify the surface brightness distribution. Others have used the *CAS* (concentration *C*, asymmetry *A*, clumpiness *S*) system (Kent 1985; Schade et al. 1995; Bershady et al. 2000; Conselice 2003). However, both the Sérsic fits and the *C* and *A* parameters of *CAS* are defined assuming that elliptical isophotes provide a good description of the objects in question. These parameters are also extremely sensitive to the precise location of the "center" of the galaxy. Given the highly irregular nature of high-redshift galaxy morphologies, it is unclear if elliptical, centroid-sensitive fits describe the galaxies in a robust and meaningful way.

Instead, we adopt a set of nonparametric coefficients to estimate galaxy morphologies. These coefficients have the advantage of not enforcing symmetries on the galaxy light distribution. The parameters we use are: size, Gini, and multiplicity.

3.1.1. *Size*

The simplest way to quantify the size of a galaxy at high redshift is by its projected (angular or physical) surface area. In particular, since the angular diameter distance in our cosmology is <10% smaller at the upper end of the BX/MD spectroscopic sample redshift distribution than at the lower end, we use the angular projected surface area as the measure of galaxy size. This is also a pragmatic choice given that we do not have spectroscopic redshifts for some of our galaxy samples. For simplicity, we define size

$$I = N_{\rm pix}, \tag{1}$$

where $N_{\rm pix}$ is the number of pixels associated with the galaxy. To convert to angular units, one must multiply I by the angular size of an ACS pixel ($[0.05'']^2$). A typical size of 250 ACS pixels corresponds to 0.625 arcsec^2, or 43 kpc^2 at $z = 2.3$.

3.1.2. *Gini*

An important measure of galaxy morphology is the distribution of light emission, in the sense that one would like to know if the galaxy surface brightness is roughly constant, or if there are large variations in surface brightness. For galaxies with a high degree of symmetry (for example, galaxies that are easily classified by the Hubble sequence), measures such as the Sérsic index or the concentration parameter *C* (proportional to the logarithm of the ratio of the radius containing 80% of the light in the galaxy to the radius containing the inner 20%) indicate the strength of variations in surface brightness. However, since high-redshift galaxies are irregular, we instead adopt the Gini parameter,

$$G = \frac{1}{\bar{X} N_{\rm pix}(N_{\rm pix} - 1)} \sum_{i=1}^{N_{\rm pix}} (2i - N_{\rm pix} - 1) X_i, \tag{2}$$

where $\bar{X}$ is the mean sky-subtracted flux per pixel, X_i is the sky-subtracted flux in pixel i, and the pixels have been sorted in order of increasing flux. This parameter, originally used in economics to describe the distribution of wealth in a population, was first used in an astronomical context by Abraham et al. (2003), and its usefulness in the context of galaxy morphology has been examined by Lotz et al. (2004, 2006) and Law et al. (2007).

Gini is defined to have a value $G = 0$ if the flux is uniformly distributed among pixels, and $G = 1$ if 1 pixel hoards all the flux in the galaxy. Thumbnails of the spectroscopic BX/MD and the DRG samples are sorted in order of increasing Gini (Figs. 2–5). Note that objects with the same Gini may span the

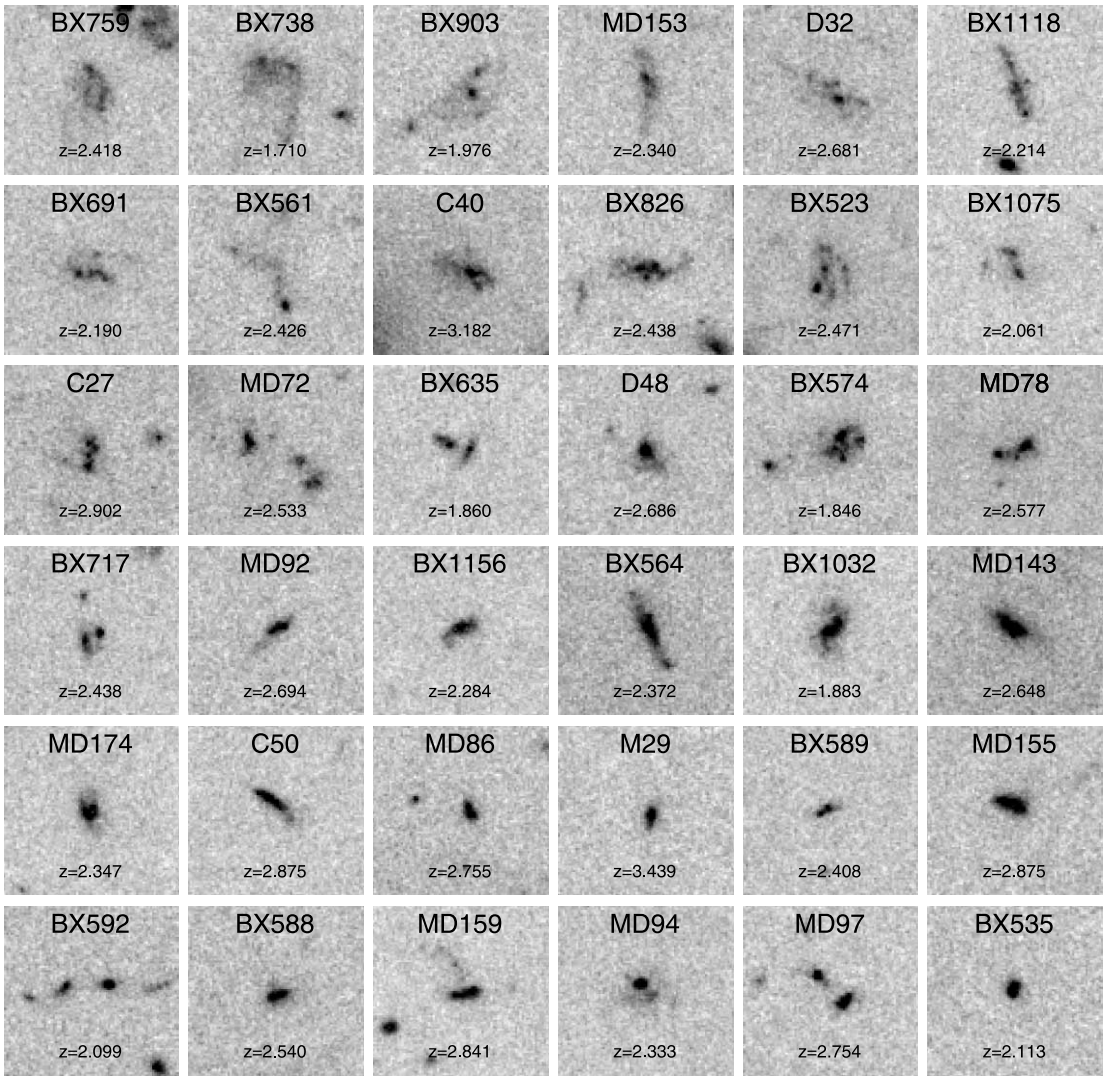

FIG. 3.—*HST* ACS images of galaxies spectroscopically confirmed not to be in the protocluster. As in Fig. 2, galaxies are sorted in order of increasing Gini, spanning the range 0.245–0.449. Images are centered on the centroids of the $\mathcal{R}$-band isophotes. See Fig. 4 for Ginis in the range 0.449–0.790.

range of diffuse objects with multiple small knots to those with a single bright central region. Therefore, unlike the Sérsic index or *C*, Gini can accommodate a wide range of spatial light distributions.

3.1.3. *Multiplicity*

In addition to describing how light is distributed among pixels, one would like to characterize the shape or clumpiness of the galaxy light distribution. We use the multiplicity (Ψ) parameter introduced by Law et al. (2007) as a measure of this property. Multiplicity is analogous to the total potential energy of a gravitational system. The total "potential energy" of the flux distribution can be described as

$$\psi_{\rm tot} = \sum_{i=1}^{N_{\rm pix}} \sum_{j=1,\, j\neq i}^{N_{\rm pix}} \frac{X_i X_j}{r_{ij}}, \tag{3}$$

where r_{ij} is the distance (in pixels) between the ith and jth pixels. If one were to reorder the pixels so that they were in the most compact configuration (i.e., with the brightest pixel at the center, and the next brightest pixels forming a ring around that pixel, and so forth), this configuration would have the greatest "total potential energy":

$$\psi_{\rm compact} = \sum_{i=1}^{N_{\rm pix}} \sum_{j=1,\, j\neq i}^{N_{\rm pix}} \frac{X_i X_j}{r'_{ij}}, \tag{4}$$

where r'_{ij} is the distance between the ith and jth particles in the new configuration. The multiplicity is then defined to be

$$\Psi = 100 \log_{10}\left(\frac{\psi_{\rm compact}}{\psi_{\rm tot}}\right). \tag{5}$$

The range of Ψ depends somewhat on the method used to assign pixels to galaxies (see § 3.2). Generally, objects with $\Psi \lesssim 2$ are bulgelike, and objects with $\Psi < 5$ tend to be dominated by one main clump. Objects with high multiplicity ($\Psi \gtrsim 15$) tend to have many almost equally bright sources that are widely separated. Galaxies with intermediate multiplicity can be highly elongated, or have several clumps that are close together. In general, galaxies that consist of several clumps of uneven luminosity will have lower multiplicity than a galaxy for which all

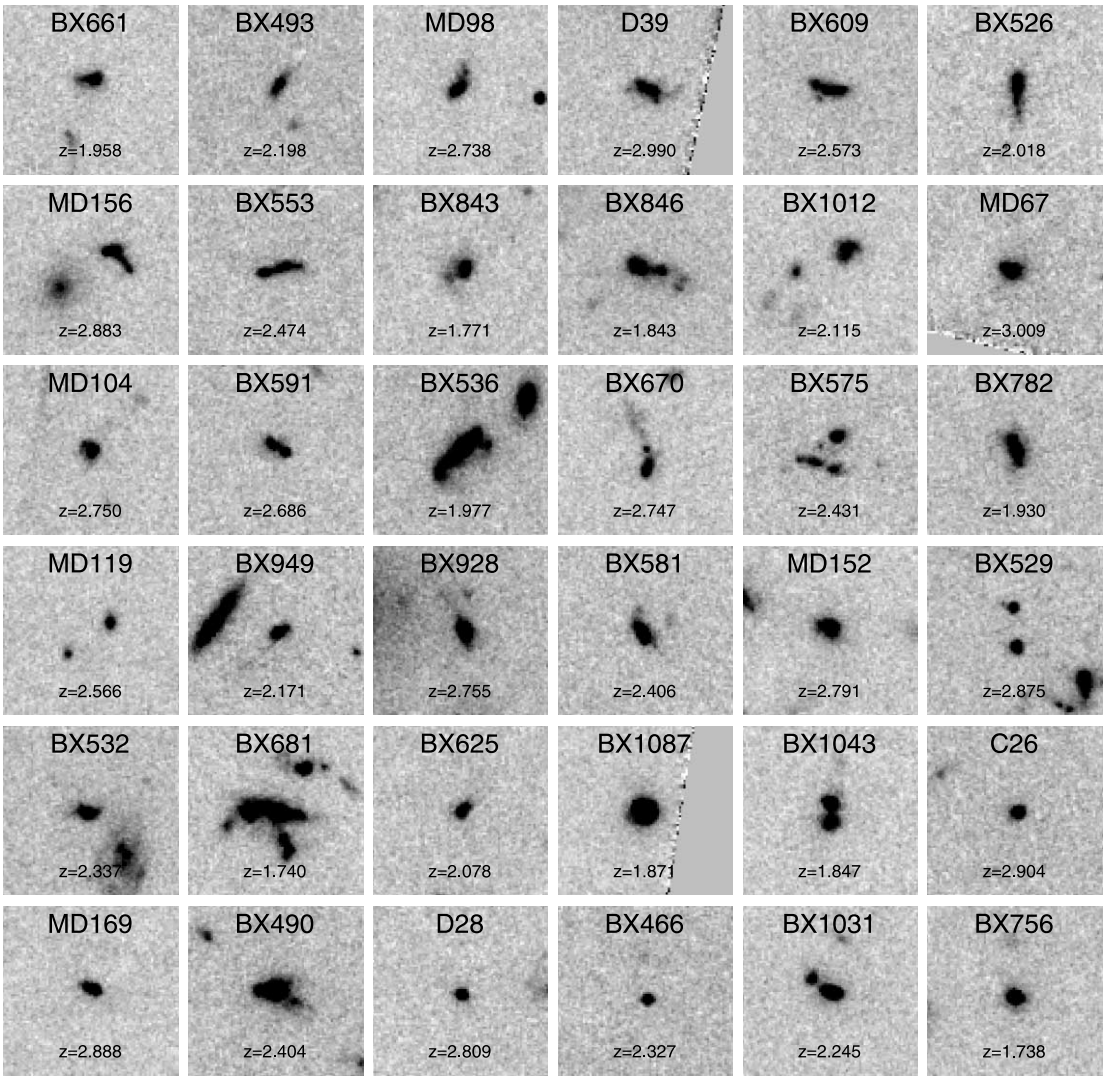

FIG. 4.—Continuation of Fig. 3. *HST* ACS images of galaxies spectroscopically confirmed to NOT be in the redshift spike. Galaxies are sorted in order of increasing Gini, spanning the range $0.449 \leq G \leq 0.790$. See Fig. 3 for galaxies with Ginis in the range 0.245–0.449.

the clumps are of approximately equal luminosity. Figure 6 demonstrates galaxies that are typical of their multiplicities.

3.2. *Pixel Selection*

A major problem in characterizing the morphologies of high-redshift galaxies is determining which pixels are associated with the galaxy, and how the pixel selection affects the quantitative measures of morphology. Lotz et al. (2004) select pixels by first determining the ellipticity and Petrosian radius of a galaxy, using elliptical apertures. They then convolve their data within the Petrosian ellipse with a Gaussian, and select all pixels within the Petrosian ellipse that meet a surface brightness cutoff. As discussed in Law et al. (2007) the caveats associated with this approach include the fact that it assumes symmetry for a population of highly irregular objects, and it tends to associate many sky pixels with the galaxy.

Law et al. (2007) use a method that does not depend on the radial symmetry of the object. An initial estimate of the galaxy centroid is obtained from ground-based imaging. The galaxy centroid is then recalculated, based on the light distribution in the ACS images. Next, an aperture of 1.5″ radius is used to search for pixels that are associated with the galaxy. Pixels are assigned with a galaxy if they meet a redshift-dependent surface brightness threshold. The redshift-dependent surface brightness threshold scales with cosmological dimming, and its purpose is to prevent bias in morphological measurements. This threshold is defined as $n(z)\sigma$, where σ is the standard deviation in the sky background. Law et al. (2007) set the threshold for the highest redshift galaxy to $n(z_{\rm high}) = 3$, where $z_{\rm high} = 3.4$. Then, since surface brightness dims as $(1+z)^{-3}$ for a fixed passband, they set the surface brightness threshold

$$n(z) = 3\left(\frac{1+z_{\rm high}}{1+z}\right)^3. \quad (6)$$

The advantage of this surface brightness threshold method is that the geometry of the object does not matter. This disadvantage of this method, for our purposes, is that it requires redshift information, which is missing for many of our galaxies, in particular, the majority of the DRGs.

For the current analysis, we adopt a pixel selection method that is redshift independent and includes all the pixels associated to the galaxy without including sky pixels. We use a redshift-independent selection method for two reasons. First, given the poor constraints on photometric redshifts, it does not make sense to use a redshift-dependent threshold based on photometric redshifts

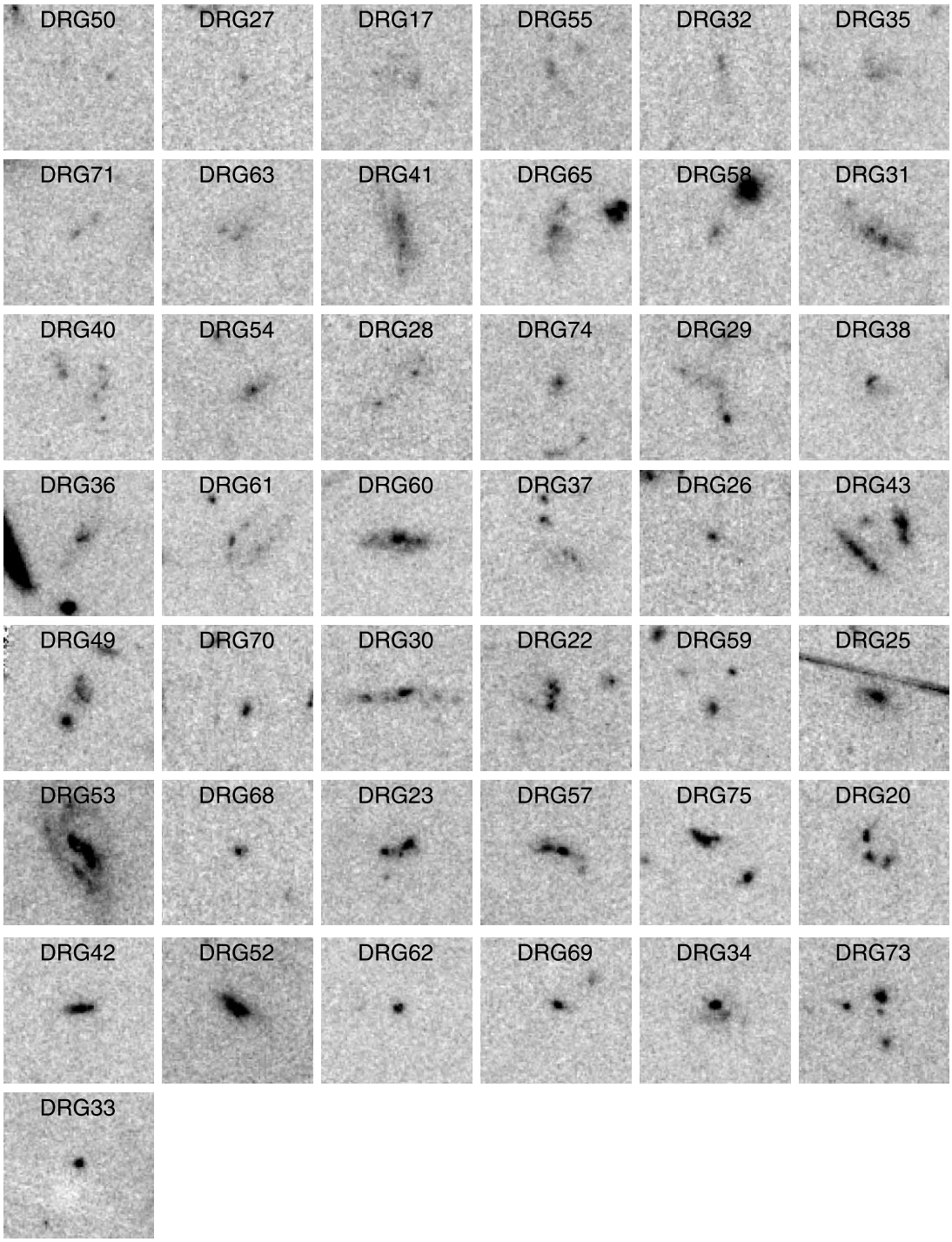

FIG. 5.—*HST* ACS images of objects satisfying the $J-K_s > 2.3$ DRG color criterion. Objects are sorted in order of increasing Gini. Images are centered at the centroid of the K_s-band isophotes.

for our samples without spectroscopic information. Second, the redshifts of our spectroscopic sample span a smaller range than those of Law et al. (2007) and Lotz et al. (2006). Lotz et al. examine two samples with mean redshifts $z \sim 1.5$ and $z \sim 4$, while Law et al. break up their $1.8 \leq z \leq 3.4$ sample into two samples with mean redshifts of $z \sim 2$ and $z \sim 3$. More than 75% of the galaxies in our BX/MD sample fall into the lower redshift bin from Law et al. (2007). Furthermore, although they span a larger redshift range than confirmed protocluster members, galaxies in the Q1700 field that are not contained within the redshift spike have a similar mean redshift, $\bar{z} = 2.34$. The similarity in the mean redshifts is due to the fact that $z = 2.3$ lies near the peak of the BX/MD redshift selection function (Steidel et al. 2004). Therefore, it is less crucial in the current study to account for cosmological dimming in the surface brightness threshold.

The first step in selecting pixels associated with a particular galaxy is to define the region in which flux could reasonably be associated with the galaxy. Like Law et al. (2007), we begin by recalculating the galaxy centroid in order to center the pixel selection region. The centroid is calculated based on the first-order moment of light on the ACS images, usually calculated within a 30 pixel (1.5″) radius circle centered on the $\mathcal{R}$-band centroid. We

TABLE 1
Galaxy Samples

Sample	Number [SEDs][a]
BX/MD spike	22 [15]
BX/MD nonspike	63 [45]
Total BX/MD w/redshift	85 [60]
BX/MD no redshift	197
Total BX/MD	282
DRG	43[b]
LBG (C/D/M) w/redshift	9 [2]
LBG (C/D/M) no redshift	26
Total LBG (C/D/M)	35

[a] SED fits were obtained for objects with near- and mid-IR imaging and spectroscopic redshift information. These are the objects used in the comparison of physical parameters and morphology.
[b] Some DRGs are also selected optically (10 total) and have spectroscopic redshifts (7 of 10); however, redshifts are not available for most of the sample.

use a different aperture within which to calculate the centroid if the multiband ground-based images indicate that there is another object (either a large foreground galaxy or a galaxy with different colors than the object in question) within the default 1.5″ aperture, or if the $\mathcal{R}$-band isophote has a linear extent >3″. In those cases, the size of the centroid-finding aperture is tailored to avoid contaminants and completely surround the $\mathcal{R}$-band detection. In some cases, a single ground-based detection will encompass several clumps of light with separations of ∼1″ (i.e., roughly the size of the ground-based seeing), which corresponds to a projected physical separation of 8 kpc at $z = 2.3$. It is highly unlikely that such small separations are the result of a projection effect, so we consider all clumps that fall within the ground-based detection isophote to be associated with each other. Therefore, we calculate the centroid for all patches of light that lie in the ground-based detection.

Next, we define an aperture about the newly calculated centroid within which we search for pixels associated with the galaxy. As in Law et al. (2007) the default aperture size is a 1.5″ radius circle. However, as in our search for the galaxy centroid, we must customize the aperture size in some cases. In those cases, we use the ground-based $\mathcal{R}$-band images as a guide, since the seeing-limited $\mathcal{R}$-band detections provide an approximate upper limit to the extent of the galaxy. If the $\mathcal{R}$-band detection extends beyond 1.5″ (∼12 kpc in projection) from the center of the object, we use a circular aperture on the ACS image that encompasses the $\mathcal{R}$-band detection. If there are foreground galaxies or objects that have significantly different colors than the object in question that lie within the default aperture, which occurs for ∼15% of the spectroscopic sample, we use circular apertures that are small enough to avoid contaminants. It was only necessary to use a noncircular aperture twice (for the photometric BX/MD sample) in order to avoid contaminants. In these cases, the elliptical apertures were aligned to the long axis of the galaxy and made large enough to encompass the whole galaxy, but small enough to avoid contaminants. The size of those elliptical apertures was also adjusted so that the total area within the aperture was not significantly different from the area of the default aperture.

As in Law et al. (2007), we perform local sky subtraction for each object to account for any imperfections in the MultiDrizzle sky subtraction. We calculate the sky background in an annulus about the detection aperture, typically 6 arcsec^2 (or ∼2400 pixels) in total surface area. We use a sigma clipping algorithm to exclude any pixels that vary by more than 3 σ about the sky level from the calculation of the sky background.

In order to determine which pixels in the detection aperture are associated with the galaxy, we convolve the data with a circularly symmetric Gaussian with a 1 pixel standard deviation, truncating the Gaussian 4 standard deviations from the center, using the IRAF tool "GAUSS." This allows us to exclude sky pixels from our segmentation map, since smoothing reduces the significance of isolated bright pixels. We select pixels to be associated with the galaxy if the smoothed flux is more than 2 σ above the sky, with σ calculated from the raw data. We then use the raw sky-subtracted flux in those pixels for our morphological analysis. In the rest of the paper, we refer to this pixel selection scheme as the "fiducial" scheme. Figure 7 shows pixels selected with both our fiducial method and the method of Law et al. (2007).

In the interest of determining the robustness of morphological parameters derived using our pixel selection scheme, we compare the values of size, Gini, multiplicity, and total flux using our pixel selection with results from various other pixel selection methods (Fig. 8). Points on Figure 8 correspond to all high-redshift galaxies with spectroscopic redshifts, including C/D/M galaxies, $z \sim 3$. We consider three reasonable schemes for selecting pixels. In scheme A, all pixels with fluxes satisfying a 5 σ threshold on the unsmoothed imaged within a 1.5″ radius of the centroid are associated with the galaxy. This allows us to evaluate the effects of smoothing for constant surface brightness selection schemes. In scheme B, we use the redshift-dependent pixel selection scheme of Law et al. (2007) to associate pixels with galaxies. This allows us to examine the effects of a redshift-dependent surface brightness threshold. In scheme C, we use the fiducial scheme with the one modification that we fix the detection aperture to 1.5″, so that we can isolate the effects of aperture size on the morphological parameters. In Figure 8, the dotted line in each panel

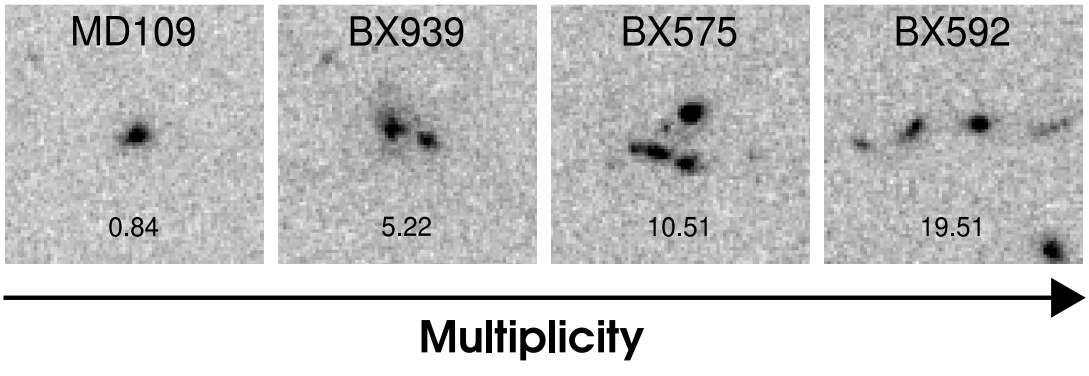

Fig. 6.—Sample galaxies (MD 109, BX 939, BX 575, and BX 592) demonstrating the range and interpretation of multiplicity.

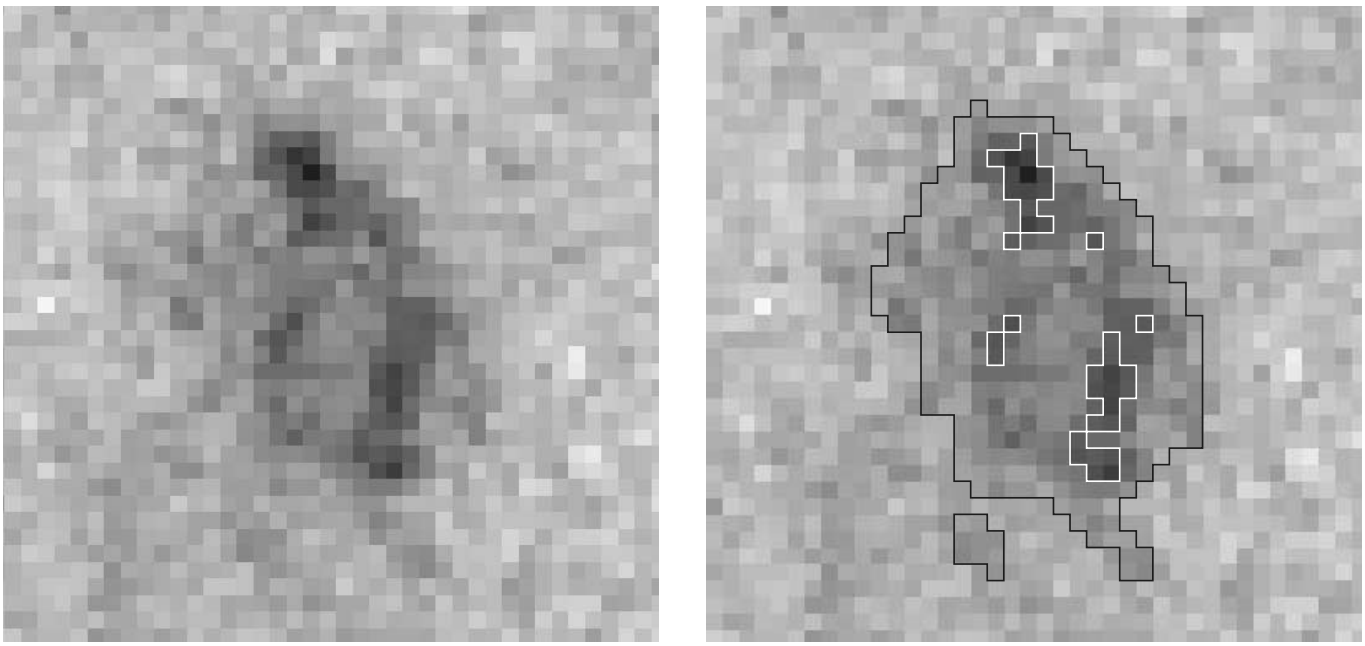

FIG. 7.—Pixel selection for BX 759 ($z = 2.418$), which would be classified as "nebulous" in Law et al. (2007). *Left*: BX 759 without pixel selections marked. Image size is $2'' \times 2''$. *Right*: White contours mark pixel selection according to the redshift-dependent pixel selection scheme of Law et al. (2007; scheme B). This corresponds to selecting all pixels >8 σ above the sky at $z = 2.418$ such that galaxies at $z_{\rm high} = 3.4$ are selected with a 3 σ surface brightness threshold. Black lines delineate the regions that are associated with the galaxy using the fiducial pixel selection scheme.

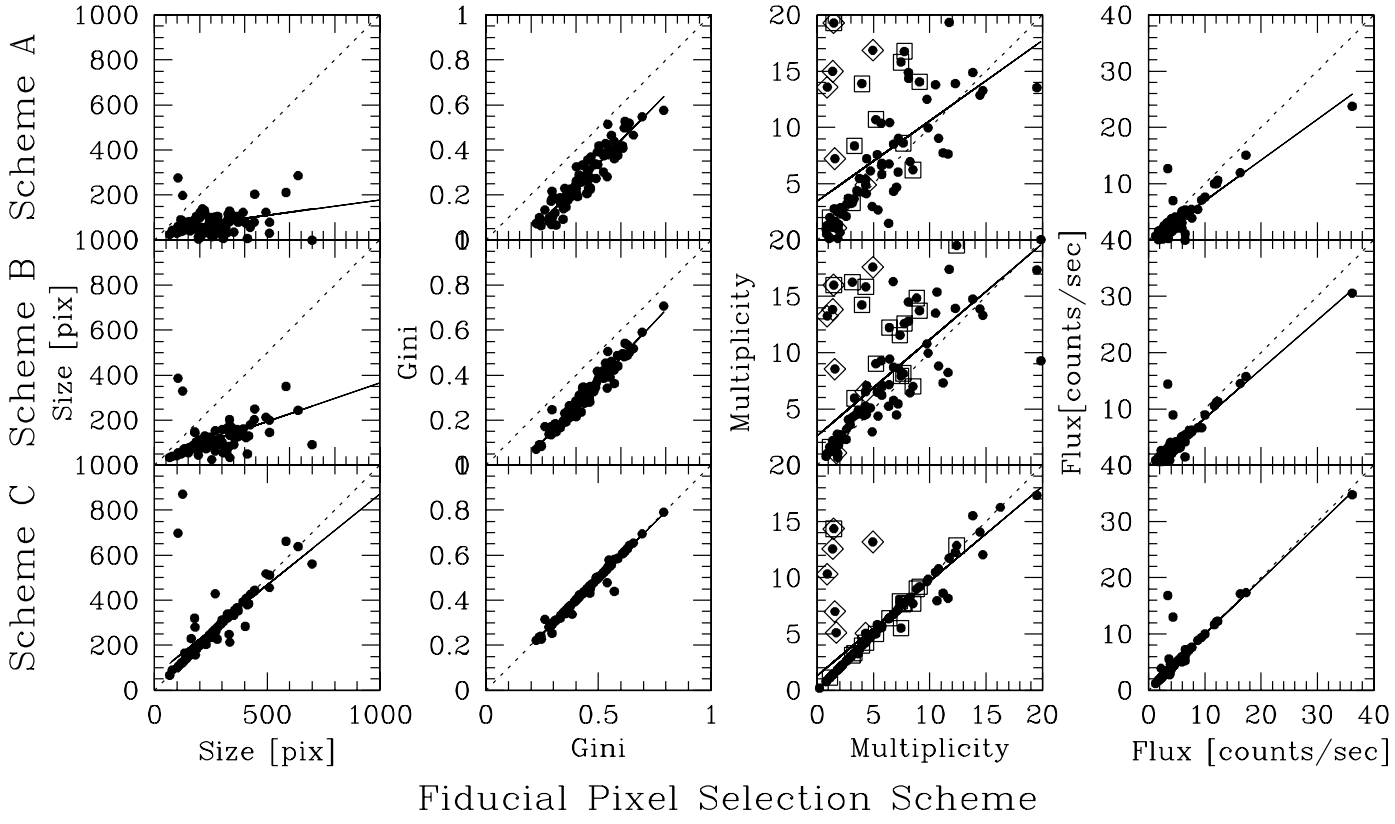

FIG. 8.—Morphological parameters as a function of pixel selection. Diamonds mark galaxies for which the 30 pixel aperture captures flux from nearby objects. Squares mark galaxies that are classified as nebulous ($G < 0.15$) by Law et al. (2007) for which multiplicity is ill-defined. [*See the electronic edition of the Journal for a color version of this figure.*]

is the line of equality ($y = x$), and the solid line is the least-squares fit to the data.

Since we are interested in the differences of the morphologies of different samples (spectroscopically confirmed protocluster and "field" BX/MDs, BX/MDs without redshifts, and DRGs), it is less important that the quantitative measures of morphology be absolutely calibrated as a function of pixel selection than it is that they be robust in a differential way. In other words, we would like a strong correlation to exist between morphological parameters calculated with two different pixel selection schemes, but it is not necessary that the parameters take the same value. We see that the sizes measured with different pixel selection schemes are well correlated (see Fig. 8), as are the Ginis and fluxes. This is especially true for scheme C, since it differs from the fiducial scheme only in the size of the detection aperture.

Multiplicity shows much more scatter than the other parameters. However, most of the scatter comes from only two effects. Points in Figure 8 outlined with diamonds represent galaxies for which the 1.5″ detection aperture includes contamination from other galaxies that are nearby in projection. Because multiplicity is sensitive to the spatial distribution of light, the effect of the contaminants is to systematically increase the multiplicity. Points outlined with squares indicate galaxies that have $G < 0.15$, as calculated in scheme B (i.e., in the fashion of Law et al. 2007), but have high multiplicity. Law et al. (2007) classify galaxies with these parameters as "nebulous," and comment that multiplicity is ill defined for these galaxies. Since they tend to have low surface brightness, they are quite sensitive to the pixel selection method. We have designed our fiducial scheme to capture as much information from these objects as possible (see Fig. 7 for an example of which pixels the fiducial scheme and scheme B select for a nebulous galaxy).

Therefore, we can conclude that, for the most part, our set of morphological parameters is robust in a differential sense to pixel selection. We use our fiducial pixel selection method throughout the paper, but will occasionally check results from the fiducial scheme against those from the other schemes.

Even for a fixed pixel selection technique, there are uncertainties in morphological parameters due to the finite signal-to-noise ratio (S/N) of the object detections. We assess such uncertainties by running simulations of our morphological analysis procedure with the fiducial pixel selection technique. Using pixel flux distributions drawn from our actual sample of objects, spanning a range of size, Gini, and multiplicity, we add copies of each object light distribution to 100 random locations in the ACS image, and recover the morphological parameters for simulated objects in relatively clean locations (i.e., objects whose fluxes are not significantly contaminated by nearby bright objects). This procedure indicates that the typical size uncertainties are 5%–10%, the typical uncertainties on Gini values are <5% [i.e., $\sigma(G) = 0.01$–0.02], and the typical multiplicity uncertainties are 5%–10%. For the faint DRGs in our sample, the uncertainties are larger, at the level of ∼15% for size, 10% for Gini [i.e., $\sigma(G) = 0.02$], and 30% for multiplicity.

4. SPIKE VERSUS NONSPIKE OBJECTS: MORPHOLOGY AS A FUNCTION OF ENVIRONMENT

Our primary interest in determining if there is a dependence of morphology on environment comes from the initial analysis of the Q1700 spike, which showed that certain properties of the spike galaxies were quite different from those not in the spike (Steidel et al. 2005). Empirically, galaxies within the spike have redder $\mathcal{R}-K_s$ colors than galaxies outside of the spike. Stellar population synthesis modeling of the broadband colors of the spectroscopically confirmed BX/MD objects showed that, regardless of whether models were fit with a constant or exponentially declining star formation rate, galaxies contained in the spike are significantly older and more massive than those not in the spike. These facts suggest that star formation history is already a function of environment at $z = 2.3$.

In this section, we consider morphology as a function of environment; in § 5 we consider morphology as a function of physical properties (mass, age, etc.) and star formation history. In this way, we can determine if environment, star formation history, and morphology are as tightly related at high redshift as they are in the current epoch. As a cautionary note, we emphasize that our data probe rest-frame UV, not optical wavelengths, and so we are probing morphologies of the young star-forming regions of each galaxy instead of the stellar mass as a whole. However, there is some evidence (Dickinson 2000; Zirm et al. 2007) that the rest-frame UV morphology is a reasonable tracer of optical morphology (but see Toft et al. 2005).

For the analysis of the morphology distributions as a function of environment, we must first define what is meant by "environment." In large surveys, such as SDSS and the DEEP2 galaxy redshift survey (Davis et al. 2003), environment refers to the number density of galaxies, as calculated on megaparsec scales. In our context, environment refers not to the local number density of galaxies, but to the binary designation of whether or not a galaxy belongs to the protocluster. We define environment in this way due to our small sample size. Therefore, we separate our spectroscopic BX/MD sample into two subsamples. The "spike" sample consists of 22 BX/MD galaxies with spectroscopic redshifts of $z = 2.300 \pm 0.015$. As shown in Figure 1 of Steidel et al. (2005), the number of galaxies in this small redshift interval exceeds the average expected number according to the BX/MD redshift selection function by a factor of $\delta_g^z \sim 7$. Typical redshift uncertainties of $\sigma_z \sim 0.002$ (Adelberger et al. 2005b) do not significantly bias the estimate of the spike overdensity. The "nonspike" sample consists of 63 spectroscopically confirmed BX/MD galaxies with $\bar{z} = 2.34$. Since we are interested in comparing the morphologies of galaxies at the same epoch but in different environments, we do not include the additional C/D/M galaxies because their high mean redshift $\bar{z} = 2.94$. The spectroscopic sample of nonspike BX/MDs serves as a good control sample due to the fact that its mean redshift is almost the same as that of the spike. We calculate the size, Gini, multiplicity, and total flux of each galaxy using the fiducial pixel selection method of § 3.

To evaluate the differences between the spike and nonspike samples in the distributions of morphological parameters (Fig. 9), we perform a one-dimensional Kolmogorov-Smirnov (K-S) test for each parameter. As demonstrated in Figure 9 and Table 2, there is no statistically significant difference between the spike and nonspike distributions for each parameter. In order to test the robustness of these findings, we perform K-S tests for a variety of pixel selection methods. Also listed in Table 2 are the K-S probabilities that the spike and nonspike morphologies are drawn from the same distribution as calculated for schemes A, B, and C. For no pixel selection method are the spike morphological parameter distributions significantly different from the nonspike distributions.

We also perform an analysis to determine if there are different proportions of "bulge-dominated" galaxies in the two samples, since, in the local universe, bulge-dominated systems (ellipticals and S0s) are preferentially found in dense environments. We define a galaxy to be bulgelike if has a multiplicity $\Psi < 2$ and $G > 0.5$, which means that it is a single compact system with a

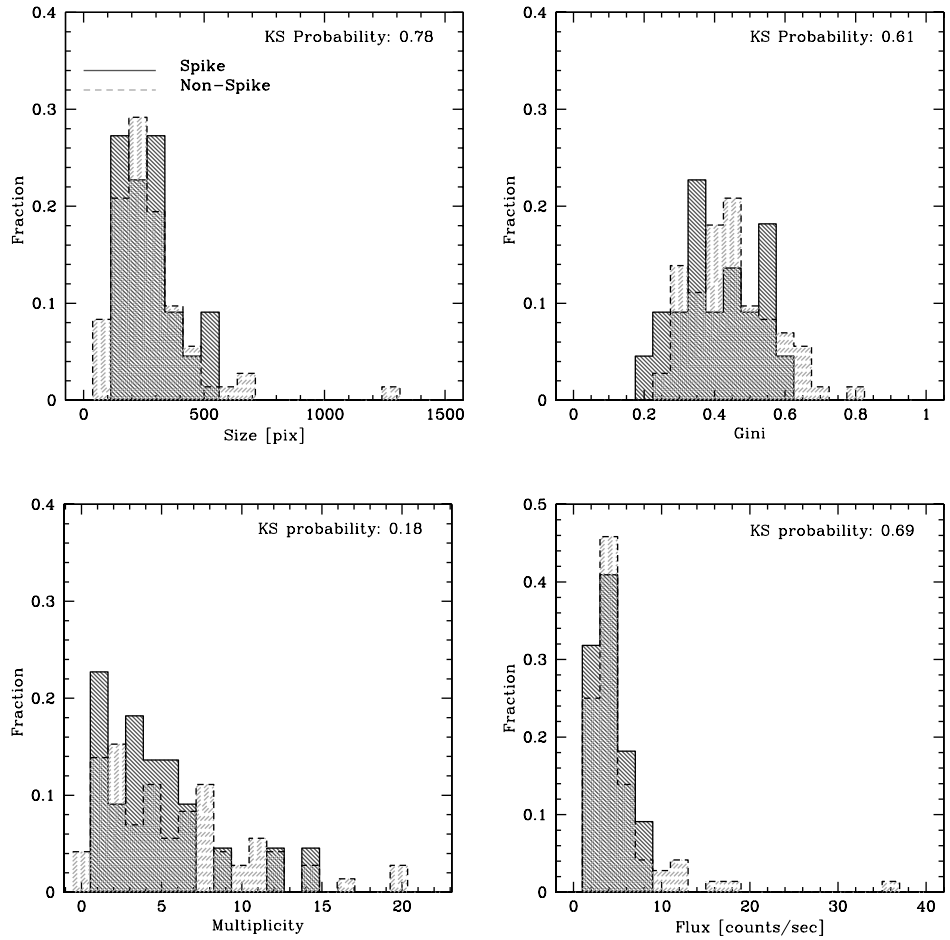

FIG. 9.—Distributions of morphological parameters (size, Gini, multiplicity, and flux). The morphology distributions of spike objects are denoted with solid lines. The distributions of the nonspike galaxies are denoted with hatched lines. The K-S probability that the distributions of spike and nonspike objects are drawn from the same distribution is located in the upper right-hand corner of each plot. [*See the electronic edition of the Journal for a color version of this figure.*]

sharply falling flux distribution function. While objects with $\Psi < 2$ are all spatially compact, they can have flux distribution functions characteristic of spheroids, exponential disks, or something in between. The cut in Gini separates galaxies with steep flux distribution functions (which would be characteristic of bulge-dominated systems) with those that have flux more uniformly distributed across pixels (typical of disklike galaxies). Separating the bulge population using cuts in two of our morphological parameters is analogous to the classification of bulges in Lotz et al. (2006) using Gini and the second moment of the light distribution. This two-dimensional classification of bulges is a cruder metric than, for example, the Sérsic index, and encodes no dynamical information. However, it is more useful if the bulk of the galaxy sample has irregular morphology, and does separate galaxies that appear to be compact and roughly axially symmetric in projection from the more irregular galaxies. Using this metric, we find that 3 of the 22 (14%) spike galaxies are bulgelike, as are 11 of the 63 (17%) nonspike objects. Given the small number of galaxies in each sample, the difference in bulge fraction is not statistically significant.

TABLE 2
K-S TEST COMPARISON OF MORPHOLOGY AND ENVIRONMENT

Pixel Selection Scheme	Size	Gini	Multiplicity	Flux
Fiducial	0.78[a]	0.61[a]	0.18[a]	0.69[a]
Scheme A	0.91	0.73	0.59	0.88
Scheme B	0.27	0.33	0.83	0.44
Scheme C	0.68	0.58	0.71	0.54

[a] The K-S probability that the spike and nonspike morphologies are drawn from the same distribution.

We invoke four arguments to explain the lack of differences in morphology between the spike and nonspike samples. The first point is that our sample size is fairly small. One can detect large differences in distributions relatively easily with small samples: for example, the large differences in the mean stellar mass of the spike and nonspike galaxy samples. However, it would be difficult to ascertain subtle differences with our small samples using the K-S test, especially if the differences were mainly in the tail of the distributions, for which the K-S test is not the optimal statistic. The second point is that, with the F814W filter, we are probing a rest-frame wavelength that is in the UV. If we are interested in morphology as a proxy for stellar mass distribution, it would be better to probe the galaxies at a rest-frame wavelength that is less sensitive to the brightest (youngest) stars and dust extinction. While several groups (e.g., Dickinson 2000; Zirm et al. 2007) claim that differences in rest-frame UV and optical morphologies are small, these conclusions are based on very small samples imaged with NIC3 (Near-Infrared Camera 3) on *HST*, which has a coarser resolution (0.26″) than that of ACS. Third, we have analyzed the morphologies of galaxies that were

photometrically selected to be star-forming and relatively unobscured. Hence, we are missing populations of old or obscured galaxies from our analysis; one might worry that we are doing the equivalent of measuring the morphologies of only spiral and irregular star-forming galaxies in the local universe. Therefore, according to these arguments, there could still be real differences in the spike and nonspike morphology distributions even though we do not detect significant evidence of differentiation with our analysis.

The fourth point is that, since the galaxies must be young (as indicated by their high redshift and stellar ages, typically $\sim$100 Myr–1 Gyr), they may not have had time to settle into dynamical equilibrium. Studies of galaxies forming by monolithic collapse (Katz & Gunn 1991; Katz 1992; Immeli et al. 2004) or by mergers (Robertson et al. 2004) demonstrate that the timescales for galaxies to reach a recognizable disk or bulge morphology are of order gigayears. Therefore, morphology may be decoupled from star formation history at high redshift. We explore this connection in § 5.

5. MORPHOLOGY AND PHYSICAL PROPERTIES OF GALAXIES

In order to examine morphology in the context of the star formation history and physical properties of galaxies, we use properties derived from the stellar population synthesis modeling of the broadband $U_nG\mathcal{R}JK_s$ + *Spitzer* IRAC photometry performed by Shapley et al. (2005) and Erb et al. (2006). These parameters include stellar mass, age, extinction, and star formation rate. In the case of Erb et al. (2006), K_s-band magnitudes are corrected for the Hα emission line. Stellar population parameters were only estimated for galaxies with both spectroscopic redshifts and near-IR photometry. The criterion on the redshifts was imposed because simultaneous fitting of photometric redshifts and star formation history leads to large uncertainties in both the photometric redshifts (typically $|z_{\rm spec} - z_{\rm phot}| = 0.3$) and stellar population model parameters (Shapley et al. 2005; van Dokkum et al. 2006). It is necessary to have near-IR photometry because near-IR bands lie on the red side of the age-sensitive 4000 Å and Balmer break features, and hence, are crucial in separating young from old stellar populations. There is a total of 60 BX/MD objects on the ACS pointings that satisfy both observational requirements, including 22 spike galaxies.

5.1. *Methods: Stellar Population Synthesis Models and Statistical Tests*

The details of population synthesis modeling are described in Shapley et al. (2005) and Erb et al. (2006). Briefly, theoretical spectral energy distributions (SEDs) are derived assuming solar metallicity and a Chabrier (2003) initial mass function (Bruzual & Charlot 2003). Starlight is attenuated with the Calzetti et al. (2000) dust attenuation model, which can be parameterized in terms of the extinction $E(B-V)$. The star formation history is assumed to be a single burst τ-model, such that the star formation rate $\mathrm{SFR}(t_{\rm sf}) = \mathrm{SFR}_0 e^{-t_{\rm sf}/\tau}$, where SFR_0 is the star formation rate at the beginning of the star-forming epoch, $t_{\rm sf}$ is the time since the beginning of star formation (i.e., it is the age of the stellar population), and τ parameterizes the length of the epoch of star formation. Constant star formation is equivalent to the statement that $\tau = \infty$. The χ^2 for each model is computed by taking the difference between the broadband photometry and the model SED.

There are several items to note for our analysis below. First, each model is parameterized by stellar age, stellar mass, SFR, extinction $E(B-V)$, and τ. Second, given the degeneracy between dust extinction and the age of the stellar population (or more generally, the star formation history), the χ^2 distribution is fairly broad for most galaxies. Fits with a constant SFR ($\tau = \infty$) are generally almost as good as the best-fit model. This means that, in general, stellar age, $E(B-V)$, SFR, and τ are loosely constrained. However, many authors (Papovich et al. 2001; Shapley et al. 2001, 2005) have shown that the assembled stellar mass is more robustly constrained. Below, we consider the model parameters of both the best-fit stellar population synthesis model and the best-fit model assuming a constant SFR.

In addition to examining the relationships between star formation history and morphology, we also investigate any connections between morphology and rest-frame UV luminosity. To determine the rest-frame UV luminosity, we use the *G*-band magnitude (centered at 4780 Å) and neglect *K*-corrections and extinction corrections. Therefore, the UV luminosity is centered at wavelengths dependent on the redshift of the object; the *G* band corresponds to a rest-frame luminosity centered at 1450 Å for the spike mean redshift of $z = 2.300$. For the range of redshifts including 80% of the BX/MD spectroscopic sample ($z = 1.9$–2.8), the *G* band probes rest-frame luminosities centered at 1650–1260 Å.

We used two different statistical measures to evaluate relationships between morphological and physical properties. For the first test, we sorted galaxies by the physical parameter in question. We then divided the galaxies into three bins, and performed one-dimensional K-S tests on the morphological distributions in the highest and lowest bins (as determined by the physical parameter). This test allows us to explore if, for example, the most massive third of galaxies have different morphology distributions than the least massive third of galaxies. Second, we performed Spearman rank correlation tests for each pair of morphological and physical parameter distributions. The results of our analysis are shown in Table 3. We quantify the results of the K-S tests in terms of the probability that the morphological distributions in the uppermost and lowermost physical parameter bins are drawn from the same distribution. We quantify the results of the Spearman test in terms of the number of standard deviations from the expectation value of the hypothesis that the data are uncorrelated.

5.2. *Morphology and Stellar Populations*

The main result from our statistical tests is that there are very few strong correlations between physical properties and morphology. First, we consider stellar mass and age, which in Steidel et al. (2005) showed significant differences in distribution as a function of environment. For both the best-fit τ and constant star formation models, age and mass are only weakly correlated with galaxy size (at the $\sim$1.5 σ level) and Gini (at slightly less than 2 σ). In Figures 10 and 11, we show scatter plots in the age-size, age-Gini, mass-size, and mass-Gini planes to demonstrate how tenuous the correlations are. Moreover, our statistical tests demonstrate that multiplicity is not well correlated with either stellar age or stellar mass. The fact that morphology correlates only weakly with stellar age and stellar mass reconciles the finding that while age and mass are strongly correlated with environment (Steidel et al. 2005), morphology is not.

Next, we comment on the extinction and SFR results. As demonstrated in Table 3, the correlation strength between morphology and $E(B-V)$ or SFR are generally weak. Moreover, the deviations from the null hypothesis that morphology and $E(B-V)$ or the SFR are uncorrelated are not always in the same direction, depending on whether the physical quantities are estimated from the best-fit τ-model or constant star formation model. The lack of consistency is a statement about the inability of the stellar

TABLE 3
CORRELATIONS OF MORPHOLOGICAL AND PHYSICAL PARAMETERS FOR BX/MD OBJECTS

	Size		Gini		Multiplicity	
Parameter	K-S[a]	N_σ[b]	K-S	N_σ	K-S	N_σ
Constant SFR						
Age	0.059142	1.20	0.275269	1.92	0.275269	−0.75
Mass	0.059142	−1.48	0.023213	1.87	0.275269	−0.96
$E(B-V)$	0.965485	−0.49	0.023213	1.19	0.059142	1.03
SFR	0.275269	−1.53	0.770953	−0.90	0.134947	1.09
Best Fit						
Age	0.134947	1.41	0.497342	1.74	0.134947	−1.08
Mass	0.023213	−1.69	0.023213	1.66	0.134947	−1.39
$E(B-V)$	0.770953	0.79	0.134947	1.01	0.002571	1.97
SFR	0.965485	1.09	0.965485	−0.67	0.275269	1.20
UV Absolute Magnitude						
	0.002929	3.73	<0.000001	5.29	0.490256	−0.33

[a] The K-S probability that the morphological parameters in the lowest physical parameter bin are drawn from the same distribution as those in the highest physical parameter bin.
[b] Number of standard deviations from the null hypothesis for the Spearman correlation test.

population synthesis models to strongly constrain the values of $E(B-V)$ and SFR. Given the large error bars on these parameters, it is also unlikely that the K-S and Spearman tests yield believable information on the strength of correlation between the $E(B-V)$ and morphology, and SFR and morphology. It should be noted that our results are in contrast with those of Law et al. (2007), who find a significant correlation between $E(B-V)$ and both size and Gini. Law et al. (2007) estimated $E(B-V)$ using best-fit τ-models. Given the uncertainty in estimating the extinction with SED fitting, especially when τ is allowed to vary, it is not so surprising that the correlation tests for these relatively small samples yield different results.

5.3. *Morphology and UV Luminosity*

We find the strongest correlations between UV luminosity (or absolute magnitude) and the morphological parameters Gini and size (Fig. 12; Table 3), while there is no evidence for a correlation between multiplicity and UV luminosity. We perform several tests to determine if the observed correlations with UV luminosity are robust. First, we perform Spearman rank correlation tests for a variety of pixel selection schemes, to ascertain that the correlations do not depend on the pixel selection method. As demonstrated in Table 4, the correlations appear to be robust to pixel selection method.

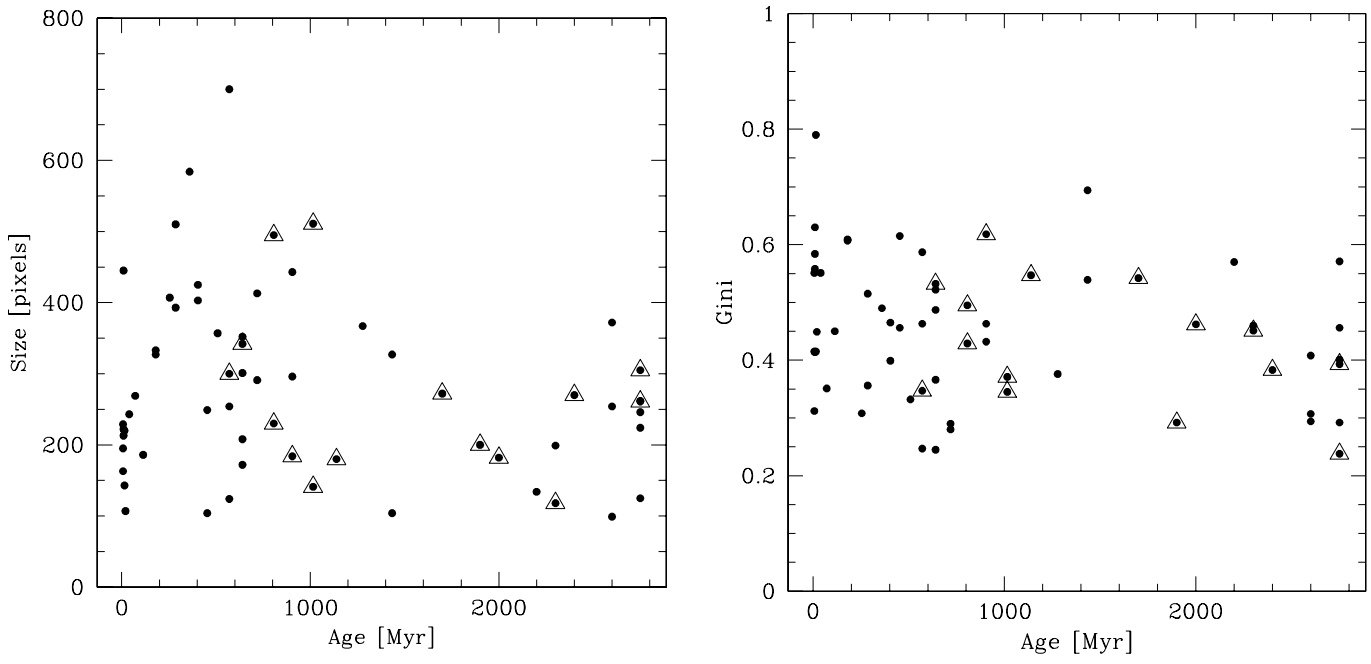

FIG. 10.—Correlations between stellar age (derived from the best-fit stellar population model with constant SFR) and morphological parameters. Triangles mark spike galaxies. *Left*: Size as a function of age. *Right*: Gini as a function of age. [*See the electronic edition of the Journal for a color version of this figure.*]

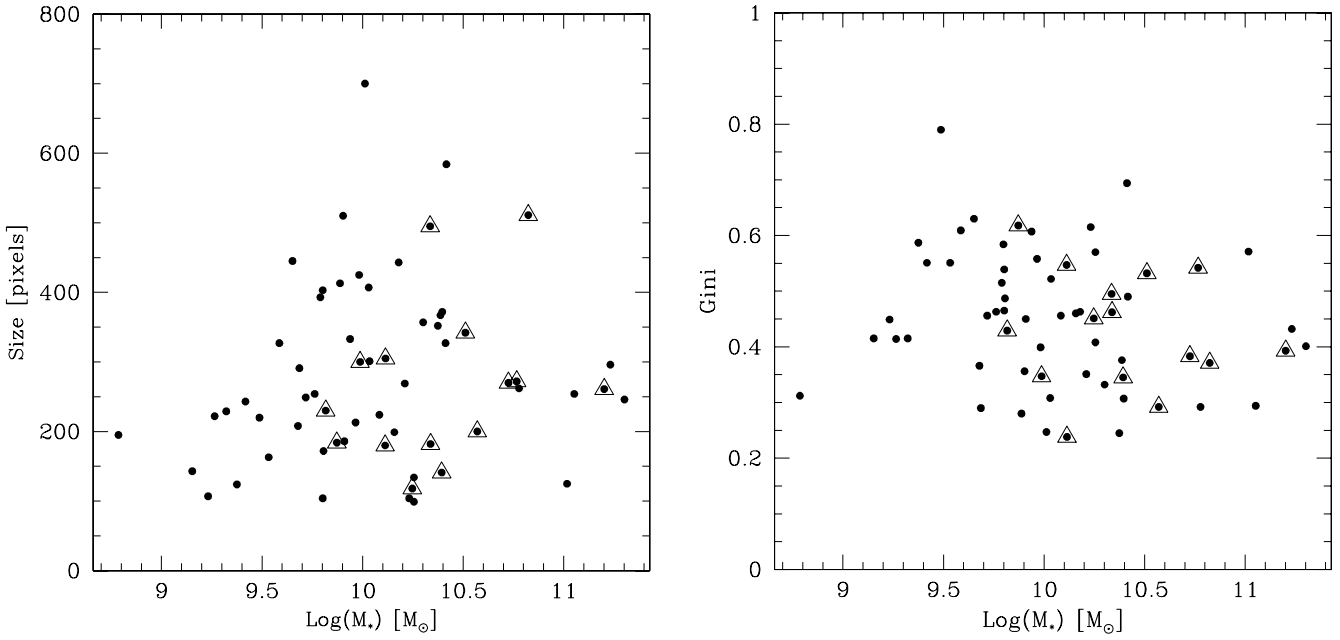

FIG. 11.—Correlations between stellar mass (derived from the best-fit stellar population model with constant SFR) and morphological parameters. Triangles mark spike galaxies. *Left*: Size as a function of mass. *Right*: Gini as a function of mass. [*See the electronic edition of the Journal for a color version of this figure.*]

Second, we consider that surface brightness–dependent pixel selection schemes might bias the luminosity-size and luminosity-Gini relationships. The fundamental reason why one ought to be concerned about surface brightness–dependent assignments to galaxies has its origin in our definitions of Gini and galaxy size. Gini is a parameter that quantifies the flux distribution function (i.e., the number of pixels of given flux). However, given that our instrument does not have infinite sensitivity, we calculate Gini with only those pixels whose surface brightness is above a certain threshold. To make an analogy with economics (the field that gave birth to the Gini coefficient), applying a surface brightness threshold cut would be the economic equivalent of including only those whose income is above the poverty line in calculating the distribution of wealth in a population. In economic literature, such a restriction on the distribution is called a "truncation bias." Since we also define size in a surface brightness–dependent way, as opposed to the traditional half-light radius, size is also subject to truncation bias.

It is important to consider what a constant surface brightness threshold means when considering galaxies with a range of luminosities. Using an economic analogy, we want to consider what Gini means if we were calculating Gini for two countries (e.g., the United States and Mexico) with different Gross Domestic Products, using incomes measured above a threshold fixed to the poverty line of one of the countries (e.g., fixing the threshold for both countries at the US poverty line). Getting back to Gini's astrophysical context, one can consider this question in a more visual way by examining the flux distribution function of

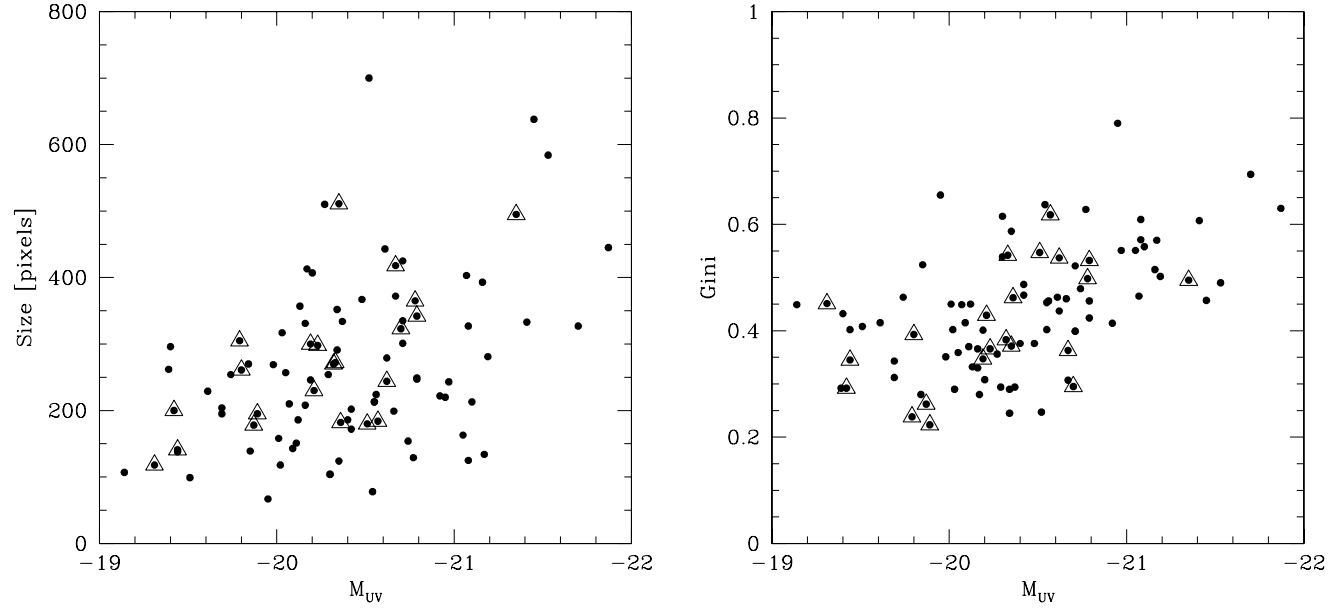

FIG. 12.—Correlation between UV absolute magnitude and galaxy size (*left*) and Gini (*right*) for the spectroscopic BX/MD sample. Triangles mark spike galaxies. [*See the electronic edition of the Journal for a color version of this figure.*]

TABLE 4
CORRELATIONS WITH UV ABSOLUTE MAGNITUDE

Scheme	Size	Gini	Multiplicity	Flux
Fiducial.....	3.73[a]	5.29[a]	−0.33[a]	7.50[a]
A.....	5.40	5.17	−1.45	7.17
B.....	6.39	5.49	−1.07	7.27
C.....	4.05	5.24	−0.23	7.26

[a] Number of standard deviations from the null hypothesis that the given parameter is uncorrelated with UV absolute magnitude, as determined by the Spearman rank correlation test.

Figure 13. If the distribution of pixels was such that the surface brightness threshold cut near the peak of the flux distribution function, one would expect the morphological parameters to deviate significantly from the values they would have had if the surface brightness threshold were lower. If two galaxies at the same redshift have flux distributions with identical shape, but different normalization (i.e., the galaxies have different luminosity), one would expect that much less of the fainter galaxy's flux distribution would meet the surface brightness criterion than the brighter galaxy's. In particular, one would expect the size of the fainter galaxy to be artificially small because fewer pixels would be associated with the galaxy. In addition, the Gini of the faint galaxy would be artificially small because the dynamic range of the fluxes in the pixels would be suppressed. In an example such as this, the ideal thing to do would be to scale the surface brightness threshold so that the threshold would apply for the same point on the flux distribution function curve, relative to the mean surface brightness, for each galaxy. This is the economic equivalent of scaling the threshold for calculating Gini by the mean income per person in each country.

In order to estimate how much Gini and size are affected by surface brightness thresholds, we focus on the ends of the luminosity distribution. The 10 lowest luminosity galaxies have a mean surface brightness of $\langle \mathrm{SB} \rangle_{\mathrm{low}} = 0.015$ counts pixel^{-1} s^{-1}, as calculated using the fiducial pixel selection method, mean Gini $\bar{G} = 0.332 \pm 0.022$,[1] and mean size $\bar{I} = 152 \pm 18$ pixels. The 10 highest luminosity galaxies had a mean surface brightness of $\langle \mathrm{SB} \rangle_{\mathrm{high}} = 0.03$ counts pixel^{-1} s^{-1}, mean Gini 0.527 ± 0.025, and mean size $\bar{I} = 447 \pm 92$ pixels, as calculated using the fiducial pixel selection method. Representative galaxies (low luminosity: BX 1030; high luminosity: BX 984) for each sample are shown in Figure 14. Since the mean surface brightness of the highest luminosity galaxies is a factor of 2 greater than the mean surface brightness, we scale the surface brightness threshold for the high-luminosity galaxies by that same factor of 2 in order to estimate the effects of truncation bias on the Gini-luminosity and size-luminosity relations. When we select pixels for the high-luminosity sample using this higher surface brightness threshold, we find that the mean Gini reduces to $\bar{G} = 0.467 \pm 0.024$, and the mean size to $\bar{I} = 292 \pm 65$ pixels (see the bottom panels of Fig. 14 for an example of how the surface brightness threshold affects size and Gini). Both the mean Gini and size of the high-luminosity sample, as calculated with the scaled surface brightness threshold, are $>1\ \sigma$ from the means of the low-luminosity sample (calculated using the default pixel selection method). This suggests that the correlation between size or Gini and luminosity is real, and not the result of truncation bias. However, we caution that the mean surface brightnesses were calculated

[1] The errors listed are the standard deviation of the mean, not the sample standard deviation.

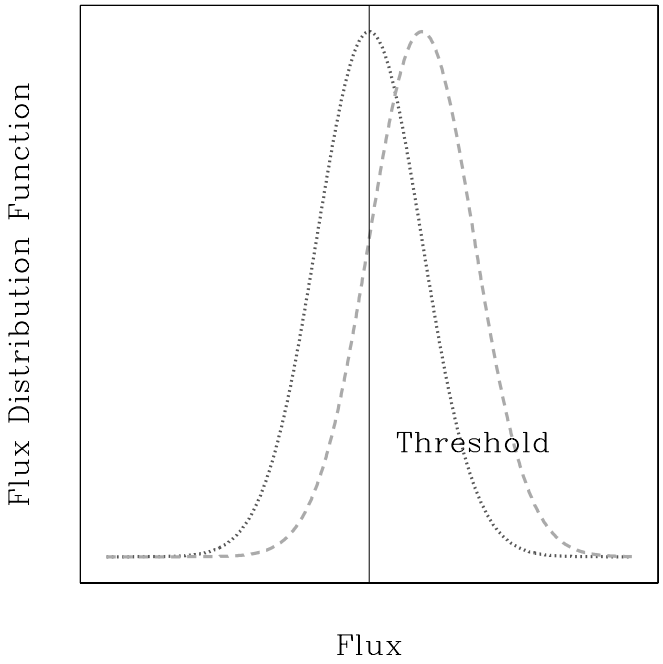

FIG. 13.—Schematic flux distribution functions for two galaxies of different luminosity, but with the same form of the distribution function. [*See the electronic edition of the Journal for a color version of this figure.*]

using only pixels that were above the surface brightness threshold, and hence the calculated mean surface brightnesses are subject to truncation bias.

We note that there is also a very tight correlation between the Gini coefficient and mean surface brightness (Fig. 15), while there is only a weak ($2\ \sigma$) anticorrelation between size and surface brightness. In order to determine if low surface brightness galaxies have artificially low Ginis due to truncation bias, we raise the surface brightness threshold of the highest surface brightness galaxies by the ratio (a factor of 4) of the mean surface brightness of the 10 highest surface brightness galaxies to the mean surface brightness of the 10 lowest surface brightness galaxies (Fig. 14). We then recalculate the Ginis of the highest surface brightness galaxies using pixels that meet the new surface brightness threshold, just as we did with luminosity. The mean Gini of the high surface brightness sample (using the fiducial pixel selection method) is 0.599 ± 0.024, and the mean Gini of the low surface brightness sample is 0.227 ± 0.009. We find that mean Gini of the highest surface brightness galaxies, calculated with the increased surface brightness threshold, decreases by $\sim$0.2 to 0.444 ± 0.026, which is not enough to destroy any of the Gini–surface brightness correlation.

The above trends are consistent with the results from simulations of our morphological analysis procedure. As described in § 3.2, in these simulations we added a series of artificial object images to the real ACS image. In this case, the artificial images consisted of the pixel light distributions for objects among the brightest in our sample, with the highest Gini vales. We then recovered the corresponding morphological parameters for simulated objects in relatively clean locations. Next, we ran the same simulations after scaling down the simulated object images by factors of 2 and 4 (roughly equivalent to lifting the surface brightness threshold by the same amount). We found that Gini and size for the scaled, fainter object images are lower by amounts consistent with what is outlined above.

Closer examination of the flux distributions demonstrate (cf. Fig. 14) that the flux distribution functions of low-Gini and

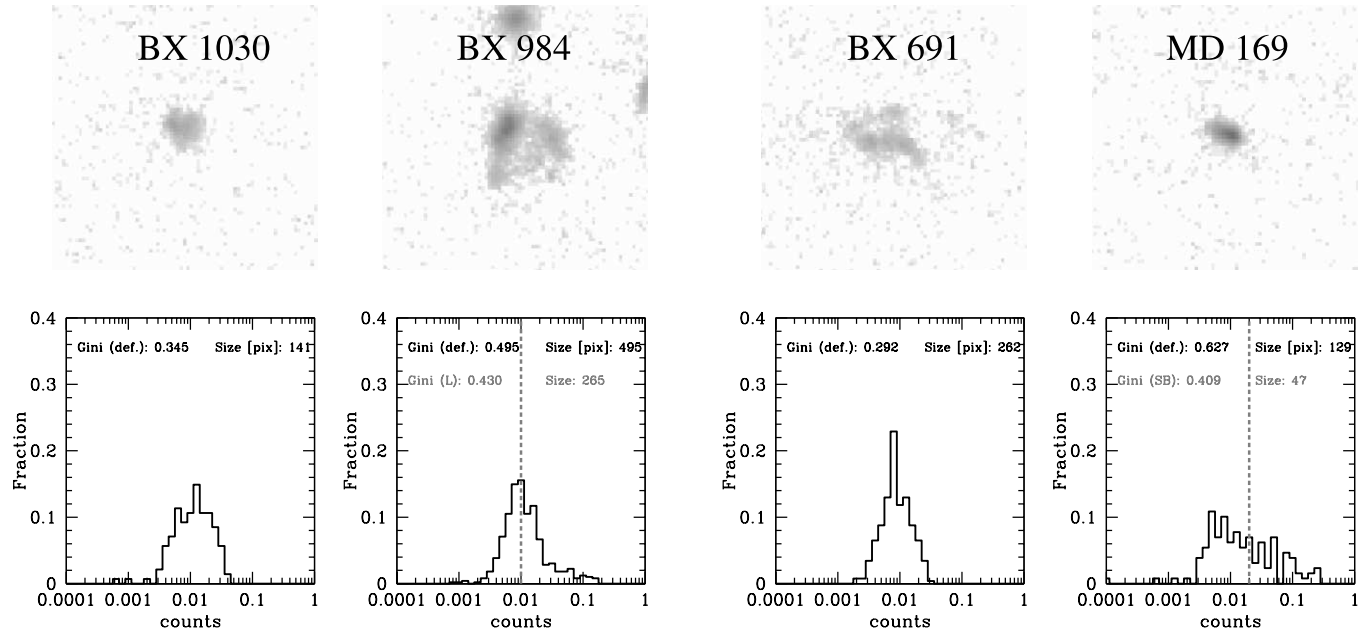

FIG. 14.— *Top panels*: *HST* ACS images of (*left to right*) the low-luminosity galaxy BX 1030, the high-luminosity galaxy BX 984, the low surface brightness galaxy BX 691, and the high surface brightness galaxy MD 169. Each galaxy has typical morphology for the galaxies within the sample (i.e., BX 1030 has typical Gini and size of the 10 lowest luminosity galaxies). The images are stretched on a logarithmic scale to match the flux distributions below. *Bottom panels*: Flux distribution functions for the galaxies above. We label the Gini and size determined with the fiducial pixel selection scheme as "default." In the leftmost two panels, we consider the effects of the surface brightness threshold on the Gini-luminosity and size-luminosity correlations. The dashed line indicates the surface brightness threshold scaled from its default value as the ratio of the mean surface brightness of the 10 most luminous galaxies to the 10 least luminous galaxies. Both Gini and size are recalculated for the typical high-luminosity galaxy BX 984 using the scaled surface brightness threshold, and are labeled "L." In the rightmost two panels, we consider the effects of the surface brightness threshold on the Gini–surface brightness and size–surface brightness correlations. The dashed line indicates the surface brightness threshold scaled from its default value as the ratio of the mean surface brightness of the 10 highest surface brightness galaxies to the 10 lowest surface brightness galaxies. Both Gini and size are recalculated for the typical high surface brightness galaxy MD 169 using the scaled surface brightness threshold, and are labeled "SB." [*See the electronic edition of the Journal for a color version of this figure.*]

high-Gini objects have fundamentally different shapes. In particular, the most luminous galaxies and those galaxies with the highest surface brightness have most of the flux concentrated in just a few pixels. This means that both the Gini coefficient and average surface brightness must necessarily be quite high for high-luminosity galaxies.

We also consider the fact that we do not *K*-correct the UV luminosities to a single wave band. Therefore, the UV luminosity we use in our analysis effectively samples the galactic SEDs at a redshift-dependent wavelength. This could affect a correlation in the following sense. If there is a tilt to the typical SED, the *G* band (from which we derive UV luminosities) will probe a different part of the SED as a function of redshift. Therefore, lower redshift galaxies could appear systematically brighter or fainter than their higher redshift counterparts. If the morphologies had a redshift dependence, this would imprint itself in the luminosity-morphology relations. In order to see if underlying size-luminosity and Gini-luminosity correlations exist if the UV luminosity samples the same part of the galaxy SED, we perform Spearman correlation tests on the spike galaxies alone. The central wavelengths for the spike range from 1442 to 1455 Å, a range much narrower than that of the entire spectroscopic BX/MD sample. Since the morphologies and luminosities of spike galaxies are not significantly different from those of field galaxies, we expect any morphology-related correlation present in the spike galaxies to also be present in the larger population. We find that, for the fiducial pixel selection scheme, size and UV luminosity are still correlated at the 2.7 σ level, and Gini and UV luminosity are correlated at the 2.5 σ level. Therefore, the UV luminosity-size and UV luminosity-Gini correlations appear to be real.

5.4. *Comparison with Recent Work*

It is useful to compare our findings to those of Law et al. (2007), whose sample of spectroscopically confirmed $z \sim 2$ BX/MD galaxies in the Great Observatories Origins Deep Survey–North (GOODS-N) has a redshift distribution that significantly overlaps with our sample. We find that, when we calculate the morphological parameters of our spectroscopic BX/MD sample in the same way as Law et al. (2007), the mean values of size, Gini, and multiplicity are almost identical to those of the $z \sim 2$ sample in the GOODS-N field.

In general, our results are consistent with those of Law et al. (2007). In particular, Law et al. (2007) also find a strong correlation between Gini and luminosity, and size and luminosity. Our results on the strength of the correlation between morphology and stellar age and mass are mildly inconsistent with Law et al. (2007), who find no correlation between stellar mass and age and morphology. We find weak evidence for correlations between stellar age and mass and morphology; however, the correlations are only marginally significant at the 1.5–2 σ level. The main difference between the two analyses lies in the relationship between extinction and morphology. Law et al. (2007) find a 3.3 σ correlation between extinction and size, and a 2.4 σ correlation between extinction and Gini. We do not find a correlation between extinction and any morphological parameter. However, the method of estimating extinction with SED fitting is subject to large errors. Therefore, the lack of consistency in the strength of the extinction-morphology relationship in the two analyses is not meaningful.

The most interesting result from this part of our analysis is that there is no strong correlation between the physical properties or

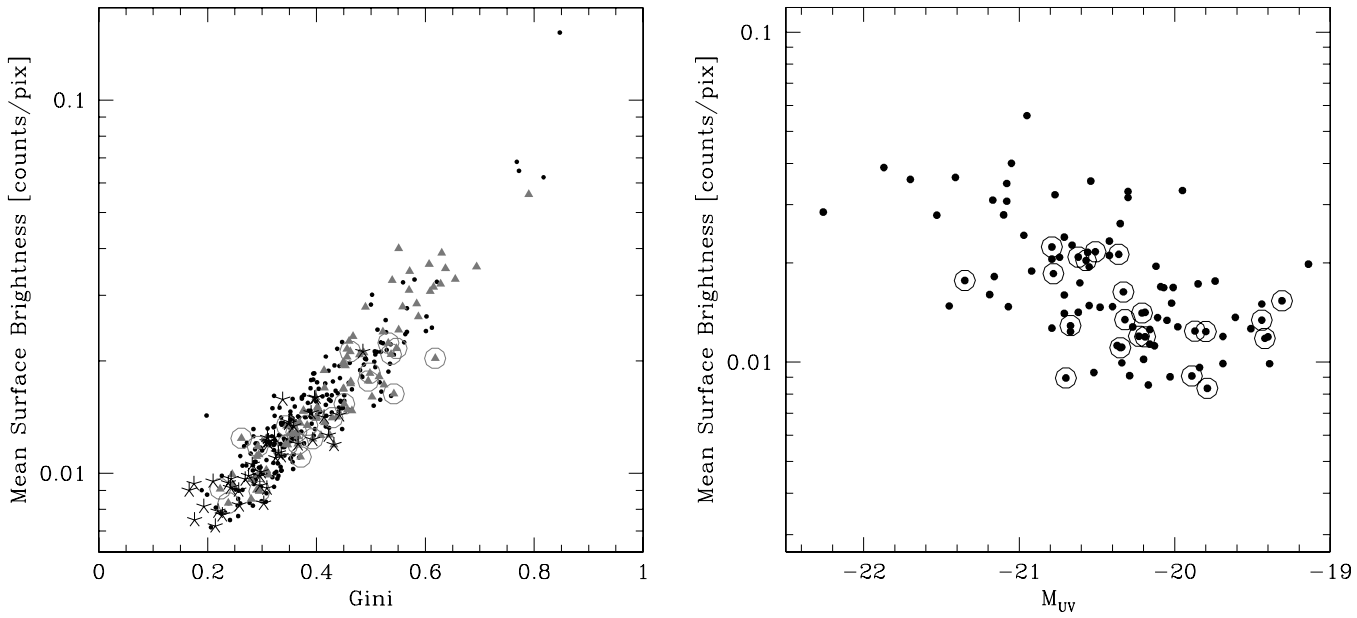

FIG. 15.—*Left*: Surface brightness as a function of Gini. The small dots denote members of the photometric BX/MD sample. Spectroscopically confirmed BX/MD galaxies are marked with larger triangles, with members of the spike outlined with circles. Asterisks mark the DRG sample. *Right*: Surface brightness as a function of UV absolute magnitude for the spectroscopic BX/MD sample. Circles outline spike galaxies. [*See the electronic edition of the Journal for a color version of this figure.*]

star formation history and galaxy morphology. This is in stark contrast to what is observed at the present epoch, where star formation history and morphology are closely tied (Kauffmann et al. 2004), although consistent with the results of Law et al. (2007).

6. MORPHOLOGIES OF OPTICAL- AND INFRARED-SELECTED GALAXIES

In addition to the sample of optically selected BX/MD galaxies, we have identified a sample of IR-selected DRGs, most of which are likely to have a similar range of redshifts as the BX/MD galaxies (Franx et al. 2003; van Dokkum et al. 2004; Kriek et al. 2006). In this section, we explore morphology as a function of galaxy selection method.

We use two samples for our morphological comparison. The first sample is the set of BX/MDs that lie on our four ACS pointings. This sample includes all photometric BX/MD candidate galaxies (including those with spectroscopic confirmation), and excludes obvious foreground objects brighter than 22 mag in the F814W filter. There is a total of 282 objects in this sample. We use this expanded sample for two reasons: it is a factor of 3 larger than the spectroscopic sample, and we want to control for the fact that the spectroscopic sample has a higher mean flux than the full sample of BX/MD galaxies, and may not be representative of the BX/MD sample as a whole. The second sample consists of 43 DRGs with $K_s \leq 21$ mag. Initial studies of DRGs selected by the criterion of $J-K_s > 2.3$ (Vega) have found a mean redshift of $\approx$2.5 (e.g., van Dokkum et al. 2003; Förster Schreiber et al. 2004). However, recent work indicates that a significant fraction of bright DRGs may be at $z < 2$ (Conselice et al. 2007; Papovich et al. 2006). This population appears to be a mix of obscured star-forming galaxies and old, passively evolving galaxies (Papovich et al. 2006).

In order to compare the two samples, we determined the mean values of the morphological parameters for each sample (Table 5), and performed a one-dimensional K-S test for each morphological parameter. We find that, although the mean object sizes of the two samples are similar, the hypothesis that the size distributions of the BX/MD and DRG samples are drawn from the same parent population is excluded at the 99.5% level. This is consistent with the findings of Law et al. (2007). As demonstrated in Figure 16, there are far more DRGs with sizes of $<$100 pixels than BX/MD galaxies. Both the mean values of Gini, multiplicity, and total flux and the K-S tests performed on these parameters indicate that the morphology distribution of the DRGs is significantly different from that of the BX/MD sample. In particular, while 55 of the 282 BX/MD galaxies have $G > 0.5$, none of the DRGs have Ginis that high. There are more high-multiplicity DRGs than BX/MDs. All of the high-multiplicity DRGs have

TABLE 5
MEAN AND 1 σ STANDARD ERRORS OF MORPHOLOGICAL PARAMETERS FOR EACH GALAXY SAMPLE

	ALL		$\langle SB \rangle < 0.01$ (counts pixel^{-1} s^{-1})		$0.01 \leq \langle SB \rangle < 0.02$ (counts pixel^{-1} s^{-1})	
PARAMETER	BX/MD	DRG	BX/MD	DRG	BX/MD	DRG
Number of galaxies	282	43	39	19	185	23
Size (pixels)	251 ± 10	215 ± 31	272 ± 23	158 ± 31	252 ± 12	269 ± 49
Gini	0.402 ± 0.006	0.308 ± 0.012	0.269 ± 0.006	0.240 ± 0.010	0.381 ± 0.005	0.356 ± 0.010
Multiplicity	6.10 ± 0.29	9.36 ± 1.05	10.44 ± 0.86	12.10 ± 1.81	6.17 ± 0.32	7.49 ± 1.06
Flux (counts s^{-1})	4.12 ± 0.23	2.51 ± 0.41	2.46 ± 0.21	1.41 ± 0.29	3.54 ± 0.16	3.49 ± 0.67
$\langle SB \rangle$ (10^{-2} counts pixel^{-1} s^{-1})	1.64 ± 0.11	1.17 ± 0.36	0.90 ± 0.11	0.89 ± 0.25	1.40 ± 0.09	1.30 ± 0.34

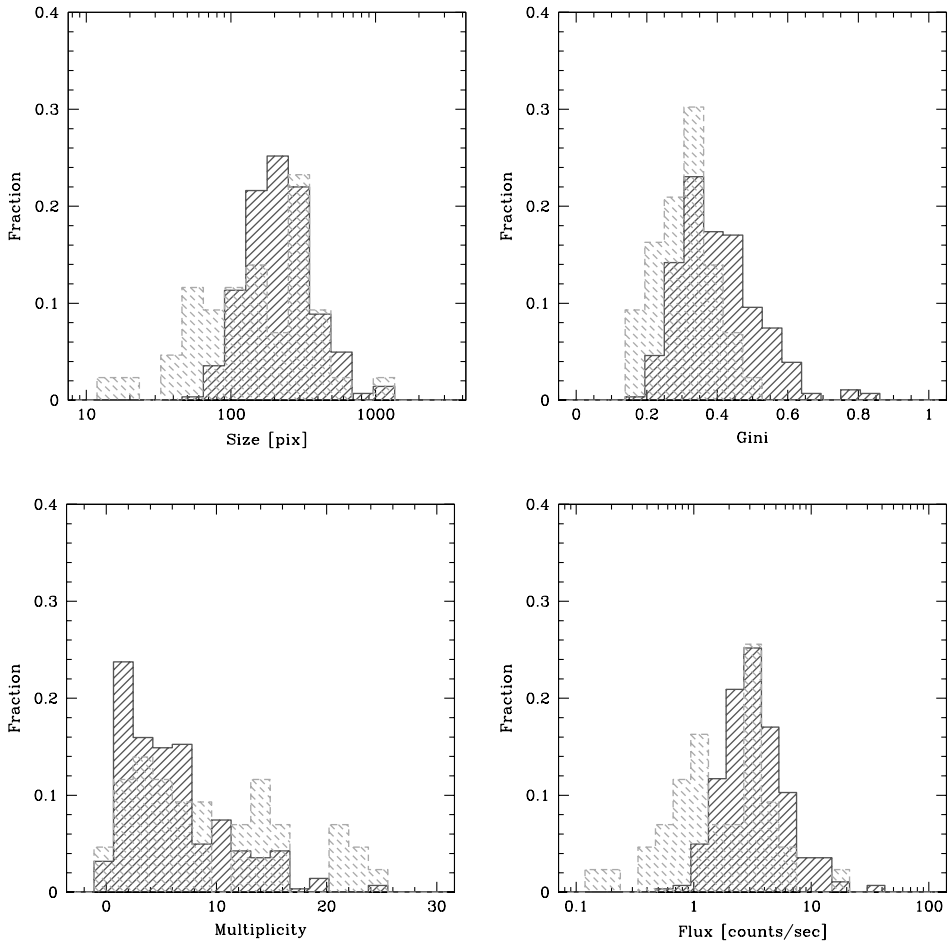

FIG. 16.—Morphology distributions for the BX/MD sample (*solid lines*) and the DRG sample (*hatched lines*). [*See the electronic edition of the Journal for a color version of this figure.*]

low surface brightness. The total fluxes of the DRGs tend to be smaller than the BX/MDs.

We would like to understand why the morphologies of the DRGs are so different from those of the BX/MDs. One concern is that the DRG sample is significantly fainter, both in terms of flux and surface brightness, than the main BX/MD sample. Of our 43 DRGs, only 17 are brighter than $\mathcal{R} = 25.5$, which is the threshold for the BX/MD sample. Of those 17 objects, 9 are also classified as BX/MDs. In § 5 we showed that UV luminosity is correlated with both size and Gini for the spectroscopic BX/MD sample. If luminosity is also correlated with morphology for the photometric BX/MDs and DRGs, then differences in the morphology distributions could be attributed to the fact that the DRG sample is fainter than the BX/MD sample. Similarly, in both samples, mean surface brightness is correlated with all morphological parameters (see Fig. 15 for the correlation with Gini), with the possible exception of galaxy size, and so it is possible that the differences in the morphology distributions can be associated with the different surface brightness distributions of the DRGs and BX/MDs.

However, we are interested in determining if there are differences in the two samples that might be due to something other than luminosity or surface brightness. In order to control for the differences in morphology between the two samples that might be attributed to differences in surface brightness, we create two subsamples with different mean surface brightness. The criterion in binning the galaxies by surface brightness is that the mean surface brightness of the BX/MD and DRG subsamples be approximately the same for each bin. Therefore, we create surface brightness bins: $\langle \mathrm{SB} \rangle < 0.01$ and $0.01 \leq \langle \mathrm{SB} \rangle < 0.02$ counts pixel^{-1} s^{-1}. We do not create any higher surface brightness bins because there is only one DRG with $\langle \mathrm{SB} \rangle > 0.02$ counts pixel^{-1} s^{-1}. We present the results of our statistical tests in Tables 5 and 6.

For the higher surface brightness bin, the K-S tests demonstrate that the hypothesis that the DRG and BX/MD morphology distributions for each parameter are drawn from the same distribution cannot be ruled out to significant confidence. However, for the lower surface brightness bin, there are some significant differences. Even though the mean surface brightness of both samples in this bin are virtually identical, the size and flux distributions are different at the 99.9% level. The DRGs are much smaller than the BX/MD galaxies. The K-S test on the Gini distributions is marginal; the null hypothesis can only be ruled out at the 90% level. The multiplicity distributions do not appear to be different to a significant level.

We would like to understand why the low surface brightness DRGs are so much smaller and fainter than the low surface brightness BX/MDs. One possible explanation lies in our choice of observed wave band. At $z \sim 2.3$, the F814W filter probes the galaxies in rest-frame UV, and hence, is sensitive to recent, relatively unobscured star formation activity. If our main interest is to use morphology to determine the distribution of star-forming

TABLE 6
K-S Test Comparison of BX/MD and DRG Morphologies

Surface Brightness Criterion	Size	Gini	Multiplicity	Flux
All	0.004549[a]	0.000021[a]	0.013885[a]	0.000003[a]
$\langle SB \rangle < 0.01$ (counts pixel^{-1} s^{-1})	0.003550	0.101108	0.193174	0.001701
$0.01 \leq \langle SB \rangle < 0.02$ (counts pixel^{-1} s^{-1})	0.514717	0.271975	0.251298	0.129829

[a] The K-S probability that the morphological parameters of BX/MD and DRG samples are drawn from the same distribution.

regions in a galaxy, the rest-frame UV may not trace the star formation of a population that consists largely of heavily obscured galaxies, such as the DRGs. It is possible that the low surface brightness DRGs have large star formation regions, but are heavily obscured by dust. DRGs with higher surface brightness could simply be less obscured. Alternatively, the low surface brightness population of DRGs might represent those galaxies that have little active star formation. In either scenario, these DRGs might appear smaller and fainter in the rest-frame UV than their low surface brightness BX/MD counterparts. With both *Spitzer* observations and spectroscopic redshifts, it will be possible to perform robust population synthesis modeling for the DRGs. Such modeling will enable estimates of star formation and extinction, and indicate the nature of these low surface brightness galaxies.

There is a possible systematic effect that might bias estimates of all of the morphological parameters. Our original justifications for using a redshift-independent surface brightness threshold for pixel selection were that the redshift distributions of our BX/MD spectroscopic and photometric samples ought be to be similar, and that we were forced to use a redshift-independent threshold, since we do not have spectroscopic redshifts for most of the DRGs. However, if the redshift distribution of the DRGs were different from that of the BX/MDs, as perhaps indicated by recent work (Conselice et al. 2007; Papovich et al. 2006; Reddy et al. 2006), it would be more prudent to use a redshift-dependent surface brightness threshold.

The main result from this section is that the UV morphologies of DRGs appear to be substantially different from those of the BX/MD star-forming sample. There are two main contributors to the overall differences in morphology. The first contributor is related to sample selection. Our two samples have different mean surface brightnesses, and morphology appears to be correlated with surface brightness for both samples. However, even if one assembled DRG and BX/MD samples of identical mean surface brightness distributions, there would be morphological differences between the samples, notably at the low end of the surface brightness distribution. At low surface brightness, the DRGs are substantially smaller and (necessarily) fainter than the BX/MDs. Without more data on the DRGs, it is not possible to determine the underlying cause of these morphological differences.

7. DISCUSSION

We have presented the first robust examination of galaxy morphological parameters as a function of environment at $z > 1.5$. In particular, optical and near-IR spectroscopic redshifts for our high-redshift galaxy candidates were a crucial component for determining whether or not the galaxies in our sample were associated with the significant overdensity at $z = 2.300 \pm 0.015$. The ability to locate these continuum-selected galaxies in redshift space sets this work apart from attempts to study galaxy properties as a function of environment in high-redshift protoclusters surrounding radio galaxies (e.g., Overzier et al. 2006; Kajisawa et al. 2006). In these studies, redshift estimates for non-Lyα-emitting galaxies were purely photometric, with associated uncertainties of $\delta(z) \geq 0.5$ (Overzier et al. 2006). Such uncertainties are too large for distinguishing between genuine protocluster membership, and chance projection.

Previous modeling of the stellar populations of $1.5 \leq z \leq 2.9$ UV-selected galaxies in the Q1700 field indicated a significantly higher mean stellar mass and age for protocluster galaxies at $z = 2.3$, relative to galaxies in less dense environments (Shapley et al. 2005; Steidel et al. 2005). The difference in mean age for protocluster galaxies is consistent with theoretical expectations that galaxy-scale overdensities should collapse earlier when located within large-scale overdensities. Along with the difference in average stellar mass and age as a function of environment, we find *no* corresponding difference in the distribution of rest-frame UV morphological properties, as described by the nonparametric Gini and multiplicity coefficients, and the angular size. We now place these results in the context of studies of galaxy properties as a function of environment spanning from the present epoch back to when the universe was roughly a third of its current age. We also highlight promising future observational and theoretical directions.

7.1. *The Lack of a Morphology-Density Relation in the Q1700 Field*

While robust environmental trends have been demonstrated in the nearby universe for both star formation history and structural parameters, we find only a connection between environment and star formation history in and around the Q1700 protocluster. There are many factors that can account for the lack of a strong connection between morphology and environment for the galaxies in our sample at $z > 1.5$. First, it is important to stress that, unlike galaxies in the local universe, for which the structural parameters and indicators of star formation history (e.g., color, 4000 Å break, and specific SFR) are tightly linked (Strateva et al. 2001), UV-selected star-forming galaxies at $z > 1.5$ do not show the same connection between structure—at least in the rest-frame UV—and star formation history. The lack of connection between morphology and star formation history has been demonstrated for spectroscopically confirmed high-redshift galaxies with modeled SEDs in the Q1700 (this work, § 5) and GOODS-N (Law et al. 2007) fields. If galaxy morphology and star formation history are uncorrelated at $z = 2.3$, and star formation history is the property most fundamentally connected with overdensity, then a strong environmental dependence of morphology should not be detected. The next significant point is that all of the morphological analysis in the Q1700 field has been performed on *HST* ACS F814W images, which probe the rest-frame UV for galaxies at $z > 1.5$. A fairer comparison with morphological studies at lower redshift, for which morphological parameters have been estimated from rest-frame optical images, will require imaging our full sample in the near-IR at high spatial resolution. Third, it has now been widely demonstrated that, unlike galaxies at $z \sim 0$–1, most of which are characterized

by well-defined centers and circularly symmetric morphologies that divide clearly into disk and bulge-dominated systems, galaxies at $z > 1.5$ generically exhibit irregular morphologies whose physical interpretation is unclear (Law et al. 2007; Lotz et al. 2006; Elmegreen et al. 2004a). Since the range of observed morphologies at $z > 1.5$ is largely disjoint with that at lower redshift, and cannot be divided into clear subsets of disk and spheroidal systems, at the very least caution should be used when searching for morphological differences as a function of environment at high redshift, in a manner analogous to low-redshift environmental analyses.

It is also important to place the photometric properties of our sample of high-redshift galaxies on the same scale as used for galaxies at lower redshift. In the analysis of the stellar populations of galaxies in the SDSS as a function of environment, Kauffmann et al. (2004) examine several properties such as optical color, 4000 Å break strength, and specific SFR. Analysis of galaxies in the $z \sim 1$ DEEP2 survey are presented in terms of the average rest-frame $U-B$ color as a function of galaxy overdensity (Cooper et al. 2006), and the average fraction of "blue" and "red" galaxies as a function of overdensity (Cooper et al. 2007) or of group versus field environment (Gerke et al. 2007). Here, blue and red refer to the two portions of the bimodal distribution of galaxy colors, observed both locally (Strateva et al. 2001) and at $z \sim 1$ (Cooper et al. 2006).

In particular, using the set of best-fit population synthesis models for UV-selected galaxies in the Q1700 field (Shapley et al. 2005), we compute the distributions of rest-frame $U-B$ color and 4000 Å break strength, $D_n(4000)$,[2] for spike and nonspike galaxies, respectively. The mean rest-frame optical color is $\langle U - B \rangle = 0.67\,[0.59]$ for spike (nonspike) galaxies, while the corresponding mean value of the 4000 Å break is $\langle D_n(4000) \rangle = 1.13\,[1.20]$. Comparison with the color-magnitude distributions presented in Cooper et al. (2007) indicates that both spike and nonspike galaxies fall squarely within the color distribution of blue galaxies in the DEEP2 sample. The $D_n(4000)$ values for both spike and nonspike galaxies are at the low extreme for galaxies in the SDSS, significantly below the transition range of $\sim$1.6–1.7, which divides the bimodal distribution of galaxy stellar populations at $z \sim 0$ (Kauffmann et al. 2003). Even the oldest galaxies in the Q1700 BX/MD sample, including those contained in the protocluster, would be classified as blue galaxies using DEEP2 and SDSS criteria. Furthermore, the stellar population differences between spike and nonspike galaxies are not significant when compared with the differences between blue and red, or early-type and late-type galaxies, in lower redshift surveys. These points are consequences of the young age of the universe at $z = 2.3$, the fact that the sample under consideration was selected in the rest-frame UV, requiring the presence of current star formation, and the fact that, at $z \sim 2$, unlike in the local universe, galaxies with stellar masses of $\sim 10^{11}\,M_\odot$ still harbor active star formation (Erb et al. 2006; Papovich et al. 2006; Reddy et al. 2006).

We must also take into account the fact that UV selection leads to an incomplete census of the range of galaxy stellar populations at $z \sim 2$ (Reddy et al. 2005; van Dokkum et al. 2006), missing galaxies with red rest-frame UV colors or faint rest-frame UV luminosities stemming from dust extinction or an evolved stellar population. It has been shown that the DRG criteria yields a sample of high-redshift galaxies largely complementary to the set of BX/MD galaxies. While the DRG sample appears to be composed of a mixture of dusty star-forming, and passive galaxies (Papovich et al. 2006), the typical stellar M/L ratio is significantly higher in this population than in the BX/MD sample. Ideally, we would like to construct complete spectroscopic samples of both BX/MD and DRG objects in the Q1700 field, and characterize the typical stellar populations and morphologies of combined BX/MD+DRG samples in both spike and nonspike environments. The associated limitation is the difficulty of obtaining spectroscopic redshifts for DRGs, which are significantly fainter in the rest-frame UV than BX/MD objects of the same mass, and characterized by lower equivalent width Hα emission in the rest-frame optical, except in the case of an active galactic nucleus (van Dokkum et al. 2004). Current and future multiobject near-IR spectrographs on 8–10 m class telescopes will aid in the effort to obtain spectroscopic redshifts for DRGs. Without spectroscopic redshifts, it will not be possible to characterize the environments of DRGs, due to the magnitude of error in typical photometric redshifts (van Dokkum et al. 2006). By including passive galaxies in the mix, we will be able to study the fraction of galaxies without ongoing star formation as a function of environment, which is more analogous to lower redshift studies of the relative fraction of blue and red galaxies than our previous investigation of blue and "slightly less blue" objects. Indeed, we have only shown so far that BX/MD galaxies in the spike appear to have started forming stars earlier than nonspike galaxies. However, since galaxies must have ongoing star formation to satisfy the BX/MD color criteria, we have little information about the past or future epoch when star formation ceases, and the related causes.

We have presented several explanations for the lack of observed dependence of BX/MD morphology on environment, including the fundamental differences between low- and high-redshift galaxy morphologies, the apparent lack of connection between irregular morphology and star formation history for UV-selected star-forming galaxies at $z \sim 2$, and the young stellar populations of all the galaxies considered here when compared with samples at lower redshift. However, other recent observations of morphologies of galaxies at similar look-back times suggest evolution in morphology as a function of *redshift*, which may also be relevant to the expected environmental dependence of morphology in high-redshift protoclusters. Indeed, Law et al. (2007) find that the mean value of the Gini coefficient is significantly higher for a sample of $z \sim 3$ LBGs, relative to that for the corresponding sample of UV-selected galaxies at $z \sim 2$, indicating more nucleated morphologies for the higher redshift sample. Estimating typical sizes of star-forming galaxies from $z \sim 1$ to $z \sim 5$, Ferguson et al. (2004) conclude that galaxies at higher redshift are smaller, at fixed luminosity. As a reflection of the acceleration of structure formation within the protocluster, Steidel et al. (2005) suggest that spike galaxies attain a level of maturity at $z \sim 2.3$, that will be reached by typical field (i.e., nonspike) galaxies at slightly lower redshift. Given the physical overdensity of the Q1700 protocluster, the morphological properties of spike galaxies should be similar to those of nonspike galaxies at $\langle z \rangle \sim 1.8$, as opposed to nonspike galaxies at $\langle z \rangle = 2.3$ (as in the current nonspike set). However, our small sample size, and the relatively small offset in effective redshift ($\Delta z \sim 0.5$), most likely prevent significant detection of differences in the average Gini or size of spike galaxies due to their lower effective redshift.

7.2. *The Existence of a Color-Density Relation in the Q1700 Field*

There are multiple lines of argument to explain the lack of difference in the distributions of rest-frame UV morphologies for

[2] This estimate of the magnitude of the 4000 Å break is used by, e.g., Kauffmann et al. (2003, 2004) for characterizing stellar populations in the SDSS, and is defined as the ratio of flux density at 4000–4100 Å to that at 3850–3950 Å.

spike and nonspike galaxies in the Q1700 field. While there is no correlation between environment and morphology for our sample of galaxies, the stellar populations of spike galaxies do appear older and more massive than those of galaxies in less dense environments. As discussed above, these differences are more subtle than the low-redshift distinction between red and blue galaxies, yet the fact remains that we do find statistically significant environmental differences in the stellar mass and age distributions. It is important to consider this result along with those from the DEEP2 survey, that the average color is redder and fraction of red galaxies is higher in group, or denser, environments at $z < 1.3$, but that there is no detectable dependence of galaxy color on local environment at $z \geq 1.3$ (Cooper et al. 2007; Gerke et al. 2007). Given the $\sim$1 Gyr timescale for galaxy colors to transform from blue to red following the cessation of star formation, the appearance of environmental trends at $z = 1.3$ indicates that the preferential formation of red galaxies in denser DEEP2 environments must commence at $z \leq 2$. For the $z = 2.3$ progenitors of the galaxies probed in the DEEP2 survey, then, no environmental trends are expected.

Our results at $z > 2$ can only be reconciled with the DEEP2 results if the galaxies in the $z = 2.3$ protocluster do not represent the progenitors of the bulk of the DEEP2 sample, but rather the progenitors of galaxies residing in richer environments by $z = 1.3$. This appears to be the case, if indeed the $z = 2.3$ protocluster virializes to become a $\sim 10^{15}\ M_{\odot}$ cluster by $z \sim 0$ (Steidel et al. 2005). We investigate this question with the aid of the Millennium Run simulation (Springel et al. 2005), a large, high-resolution *N*-body simulation of cosmic dark matter structure formation. According to dark matter halo merger trees constructed from the output of the Millennium simulation (Springel et al. 2005; Lemson et al. 2006), the typical mass ratio between a $\sim 10^{15}\ M_{\odot}$ dark matter halo at $z \sim 0$ and its most massive progenitor at $z = 1.3$ is roughly a factor of $\sim$6. Therefore, by $z = 1.3$, the Q1700 spike galaxies should be residing in a halo of mass $\sim 2 \times 10^{14}\ M_{\odot}$. The DEEP2 survey is more heavily weighted toward galaxies residing in the field or in less massive structures. The bulk of groups featured in the DEEP2 sample of Gerke et al. (2007) span the range $5 \times 10^{12} \leq M \leq 5 \times 10^{13}$, with a negligible fraction of systems with $M > 10^{14}\ M_{\odot}$. The DEEP2 sample of Cooper et al. (2006, 2007) probes a similar range of environments. Therefore, the environment of the likely $z = 1.3$ descendant of the $z = 2.3$ protocluster is not well represented within the DEEP2 environmental samples, and there is no contradiction between our observed color dependence on environment at $z = 2.3$ and the lack thereof in the DEEP2 survey at $z = 1.3$.

7.3. *Future Directions*

There are several promising theoretical and observational directions to pursue. More work is required to determine the detailed three-dimensional distribution of the protocluster galaxies, and the manner in which they are grouped. Given that the angular distribution of galaxies contained within the spike in redshift space extends over at least $\sim$11 comoving megaparsecs on the sky, and is not obviously segregated from nonspike galaxies (Steidel et al. 2005), the protocluster defined in redshift space does not constitute a single, well-defined, virialized object. Therefore, we would like to understand the mass of typical structures containing protocluster galaxies at $z = 2.3$ that will inhabit $\sim 10^{15}\ M_{\odot}$ clusters by $z \sim 0$. Based on the Millennium simulation merger trees, it appears that the $z \sim 2$ progenitor halo mass distribution of $\sim 10^{15}\ M_{\odot}$ clusters at $z \sim 0$ typically contain between one and five $\sim 10^{13}\ M_{\odot}$ dark matter halos. Since the dark matter halo mass in which a galaxy resides affects the amount and fate of mass and gas it accretes (Kereš et al. 2005; Dekel & Birnboim 2006), a careful understanding of the way in which protocluster galaxies populate dark matter halos at $z \sim 2$ will shed light on their future star formation histories. While detailed dark matter plus hydrodynamics simulations of massive cluster formation (Kravtsov et al. 2005) have been performed, most of the close comparisons with observations have been tuned to $z \sim 0$. We would also like to employ a close comparison of the detailed star formation histories and structures of simulated protocluster and field galaxies prior to $z = 2.3$.

Furthermore, future morphological studies of statistical samples of $z \sim 2$ in the rest-frame optical will provide a cleaner view of galaxy structure. The camera currently on *HST* with the minimum acceptable angular resolution for this type of study is NIC2 (Near-Infrared Camera 2) on NICMOS (Near-Infrared Camera and Multi-Object Spectrometer), although its small field of view provides a survey efficiency too low for building up a statistical sample of rest-frame optical morphologies. However, the WFC3 (Wide Field Camera 3), to be installed in *HST* during Servicing Mission 4, will enable this type of study in future years. Our detailed observations of the environment of the Q1700 protocluster, plus a close comparison with simulations of cluster formation tuned to $z = 2.3$, will provide a unique opportunity to learn about the seeds of the environmental dependence of galaxy properties.

Based on observations made with the NASA ESA *Hubble Space Telescope*, obtained at the Space Telescope Science Institute, which is operated by the Association of Universities for Research in Astronomy, Inc., under NASA contract NAS 5-26555. These observations are associated with program HST-GO-10581.07-A. Support for program HST-GO-10581.07-A was provided by NASA through a grant from the Space Telescope Science Institute, which is operated by the Association of Universities for Research in Astronomy, Inc., under NASA contract NAS 5-26555. A. E. S. acknowledges support from the David and Lucile Packard Foundation. C. C. S. and D. R. L have been supported by grants AST 06-06912 from the US National Science Foundation and HST-AR-10311 from NASA through the Space Telescope Science Institute. We thank Jennifer Lotz for providing us with her morphological analysis of the GOODS-N field, Mauro Giavalisco for useful discussions, and an anonymous referee, whose comments improved the paper.

REFERENCES

Abadi, M. G., Moore, B., & Bower, R. G. 1999, MNRAS, 308, 947
Abraham, R. G., van den Bergh, S., & Nair, P. 2003, ApJ, 588, 218
Adelberger, K. L., Erb, D. K., Steidel, C. C., Reddy, N. A., Pettini, M., & Shapley, A. E. 2005a, ApJ, 620, L75
Adelberger, K. L., Shapley, A. E., Steidel, C. C., Pettini, M., Erb, D. K., & Reddy, N. A. 2005b, ApJ, 629, 636
Adelberger, K. L., Steidel, C. C., Shapley, A. E., Hunt, M. P., Erb, D. K., Reddy, N. A., & Pettini, M. 2004, ApJ, 607, 226
Barmby, P., et al. 2004, ApJS, 154, 97
Bekki, K., Couch, W. J., & Shioya, Y. 2002, ApJ, 577, 651
Benson, A. J., Ellis, R. S., & Menanteau, F. 2002, MNRAS, 336, 564
Benson, A. J., Frenk, C. S., Baugh, C. M., Cole, S., & Lacey, C. G. 2001, MNRAS, 327, 1041
Bershady, M. A., Jangren, A., & Conselice, C. J. 2000, AJ, 119, 2645
Blanton, M. R., Eisenstein, D., Hogg, D. W., Schlegel, D. J., & Brinkmann, J. 2005, ApJ, 629, 143

Bruzual, G., & Charlot, S. 2003, MNRAS, 344, 1000
Calzetti, D., Armus, L., Bohlin, R. C., Kinney, A. L., Koornneef, J., & Storchi-Bergmann, T. 2000, ApJ, 533, 682
Chabrier, G. 2003, PASP, 115, 763
Conselice, C. J. 2003, ApJS, 147, 1
Conselice, C. J., et al. 2007, ApJ, 660, L55
Cooper, M. C., et al. 2006, MNRAS, 370, 198
———. 2007, MNRAS, 376, 1445
Croton, D. J., et al. 2006, MNRAS, 365, 11
Davis, M., et al. 2003, Proc. SPIE, 4834, 161
De Breuck, C., van Breugel, W., Röttgering, H. J. A., & Miley, G. 2000, A&AS, 143, 303
Dekel, A., & Birnboim, Y. 2006, MNRAS, 368, 2
Dickinson, M. 2000, Philos. Trans. R. Soc. London, A, 358, 2001
Dressler, A. 1980, ApJ, 236, 351
Elmegreen, D. M., Elmegreen, B. G., & Hirst, A. C. 2004a, ApJ, 604, L21
Elmegreen, D. M., Elmegreen, B. G., & Sheets, C. M. 2004b, ApJ, 603, 74
Erb, D. K., Steidel, C. C., Shapley, A. E., Pettini, M., Reddy, N. A., & Adelberger, K. L. 2006, ApJ, 646, 107
Ferguson, H. C., et al. 2004, ApJ, 600, L107
Förster Schreiber, N. M., et al. 2004, ApJ, 616, 40
Franx, M., et al. 2003, ApJ, 587, L79
Gerke, B. F., et al. 2007, MNRAS, 376, 1425
Goto, T., Yamauchi, C., Fujita, Y., Okamura, S., Sekiguchi, M., Smail, I., Bernardi, M., & Gomez, P. L. 2003, MNRAS, 346, 601
Gunn, J. E., & Gott, J. R. I. 1972, ApJ, 176, 1
Hester, J. A. 2006, ApJ, 647, 910
Immeli, A., Samland, M., Westera, P., & Gerhard, O. 2004, ApJ, 611, 20
Jenkins, A., et al. 1998, ApJ, 499, 20
Kajisawa, M., Kodama, T., Tanaka, I., Yamada, T., & Bower, R. 2006, MNRAS, 371, 577
Katz, N. 1992, ApJ, 391, 502
Katz, N., & Gunn, J. E. 1991, ApJ, 377, 365
Kauffmann, G., Colberg, J. M., Diaferio, A., & White, S. D. M. 1999, MNRAS, 303, 188
Kauffmann, G., White, S. D. M., Heckman, T. M., Ménard, B., Brinchmann, J., Charlot, S., Tremonti, C., & Brinkmann, J. 2004, MNRAS, 353, 713
Kauffmann, G., et al. 2003, MNRAS, 341, 33
Kent, S. M. 1985, ApJS, 59, 115
Kereš, D., Katz, N., Weinberg, D. H., & Davé, R. 2005, MNRAS, 363, 2
Koekemoer, A. M., Fruchter, A. S., Hook, R. N., & Hack, W. 2002, in *HST* Calibration Workshop: *Hubble* after the Installation of the ACS and the NICMOS Cooling System, ed. S. Arribas, A. Koekemoer, & B. Whitmore (Baltimore: STScI), 337
Kravtsov, A. V., Nagai, D., & Vikhlinin, A. A. 2005, ApJ, 625, 588
Kriek, M., et al. 2006, ApJ, 649, L71
Kurk, J. D., Venemans, B. P., Röttgering, H. J. A., Miley, G. K., & Pentericci, L. 2002, in ASP Conf. Ser. 268, Tracing Cosmic Evolution with Galaxy Clusters, ed. S. Borgani, M. Mezzetti, & R. Valdarnini (San Francisco: ASP), 23
Larson, R. B., Tinsley, B. M., & Caldwell, C. N. 1980, ApJ, 237, 692
Law, D. R., Steidel, C. C., Erb, D. K., Pettini, M., Reddy, N. A., Shapley, A. E., Adelberger, K. L., & Simenc, D. J. 2007, ApJ, 656, 1
Lemson, G., et al. 2006, preprint (astro-ph/0608019)
Lotz, J. M., Madau, P., Giavalisco, M., Primack, J., & Ferguson, H. C. 2006, ApJ, 636, 592
Lotz, J. M., Primack, J., & Madau, P. 2004, AJ, 128, 163
Maulbetsch, C., Avila-Reese, V., Colín, P., Gottlöber, S., Khalatyan, A., & Steinmetz, M. 2007, ApJ, 654, 53
Moore, B., Katz, N., Lake, G., Dressler, A., & Oemler, A., Jr. 1996, Nature, 379, 613
Moore, B., Lake, G., Quinn, T., & Stadel, J. 1999, MNRAS, 304, 465
Mullis, C. R., et al. 2003, ApJ, 594, 154
Okamoto, T., & Nagashima, M. 2001, ApJ, 547, 109
Overzier, R. A., et al. 2006, ApJ, submitted (astro-ph/0601223)
Papovich, C., Dickinson, M., & Ferguson, H. C. 2001, ApJ, 559, 620
Papovich, C., et al. 2006, ApJ, 640, 92
Pascarelle, S. M., Windhorst, R. A., Keel, W. C., & Odewahn, S. C. 1996, Nature, 383, 45
Postman, M., & Geller, M. J. 1984, ApJ, 281, 95
Postman, M., et al. 2005, ApJ, 623, 721
Quadri, R., et al. 2007, ApJ, 654, 138
Ravindranath, S., et al. 2006, ApJ, 652, 963
Reddy, N. A., Erb, D. K., Steidel, C. C., Shapley, A. E., Adelberger, K. L., & Pettini, M. 2005, ApJ, 633, 748
Reddy, N. A., Steidel, C. C., Fadda, D., Yan, L., Pettini, M., Shapley, A. E., Erb, D. K., & Adelberger, K. L. 2006, ApJ, 644, 792
Robertson, B., Yoshida, N., Springel, V., & Hernquist, L. 2004, ApJ, 606, 32
Schade, D., Lilly, S. J., Crampton, D., Hammer, F., Le Fevre, O., & Tresse, L. 1995, ApJ, 451, L1
Shapley, A. E., Steidel, C. C., Adelberger, K. L., Dickinson, M., Giavalisco, M., & Pettini, M. 2001, ApJ, 562, 95
Shapley, A. E., Steidel, C. C., Erb, D. K., Reddy, N. A., Adelberger, K. L., Pettini, M., Barmby, P., & Huang, J. 2005, ApJ, 626, 698
Smith, G. P., Treu, T., Ellis, R. S., Moran, S. M., & Dressler, A. 2005, ApJ, 620, 78
Springel, V., et al. 2005, Nature, 435, 629
Steidel, C. C., Adelberger, K. L., Dickinson, M., Giavalisco, M., Pettini, M., & Kellogg, M. 1998, ApJ, 492, 428
Steidel, C. C., Adelberger, K. L., Shapley, A. E., Erb, D. K., Reddy, N. A., & Pettini, M. 2005, ApJ, 626, 44
Steidel, C. C., Adelberger, K. L., Shapley, A. E., Pettini, M., Dickinson, M., & Giavalisco, M. 2003, ApJ, 592, 728
Steidel, C. C., Shapley, A. E., Pettini, M., Adelberger, K. L., Erb, D. K., Reddy, N. A., & Hunt, M. P. 2004, ApJ, 604, 534
Strateva, I., et al. 2001, AJ, 122, 1861
Toft, S., van Dokkum, P., Franx, M., Thompson, R. I., Illingworth, G. D., Bouwens, R. J., & Kriek, M. 2005, ApJ, 624, L9
van Dokkum, P. G., et al. 2003, ApJ, 587, L83
———. 2004, ApJ, 611, 703
———. 2006, ApJ, 638, L59
Zirm, A. W., et al. 2007, ApJ, 656, 66